June 2015

Surface Plasmon Polaritons: Guided-wave Devices and Applications

Ashish Chanana
Syracuse University

Abstract

The prospect of controlling the interaction of light with matter at nanoscale has been widely studied in recent years, and entails characterizing optical and optoelectronic devices at resolution higher than the diffraction limit. One technique that allows localization of light to sub-wavelength dimensions is through the use of surface plasmon polaritons (SPPs) wherein the interaction of light with free electrons on a metal surface can lead to a bound surface electromagnetic field that is confined to deep sub-wavelength dimensions. Studies based on SPPs merged with the field of nanotechnology have resulted in novel imaging technologies, nonlinear and quantum-optical devices and the ability to design materials with unusual electromagnetic properties with potential applications ranging from enhancing the efficiency of photovoltaic devices to detection of bio-molecules at ultra-small concentrations.

Here we report the design of nanophotonic devices based on SPP waveguide structures that would act as a true counterpart to today's electronic devices, providing orders of increase in data speeds while maintaining nanoscale dimensions. The devices are based on metal-dielectric-metal (MDM) waveguide structures composed of $Ag/SiO_2/Ag$ heterostructure that utilizes interference effect within multiple intersecting plasmonic waveguides. We have explored guided-wave devices such as L and T-bends, 4-way-splitters and 2x2-networked structures, wherein by altering the device geometry one can tune its operating frequency, and by changing the angle of incidence one can switch these devices between ON/OFF states. We plan to fabricate and experimentally characterize these devices for applications in color routing, directional filters and optical switches. We discuss preliminary design rules and constraints based on results obtained from finite-difference-time-domain simulations.

Surface Plasmon Polaritons: Guided-Wave Devices and Applications

by

Ashish Chanana

B.Tech, Maharshi Dayanand University, 2011

Thesis

Submitted in partial fulfillment of the requirements for the degree of
Master of Science in Electrical Engineering in the Graduate School
of Syracuse University

June 2015

Acknowledgement

First of all, I would like to express my sincere gratitude towards my advisors Dr. Jay K. Lee and Dr. Amit Agrawal for their unending support and valuable guidance throughout my course of graduate studies. I would like to thank them for providing me with continuous feedback through theoretical, writing and editing process. I am thankful to Dr. Agrawal for providing me opportunity to work on the thesis and in the nanophotonics lab with him. I would also like to thank Matthew Davis for useful discussions and his support with experiments.

During the course of graduate studies I had opportunity to work and study with very talented and helpful friends. I am thankful to them for their support and keeping me company.

Table of Contents

List of Figures:

1. Introduction

This thesis is a step toward the investigation of light-matter interaction at the nanoscale. At sub wavelength scale light-matter interaction is limited by diffraction, which restricts us to application of optics to wavelength scale. The diffraction limit poses a major challenge and restricts our capability to resolve two features under the microscope with separation below the Abbe's diffraction limit of $\lambda/2n$ for light with wavelength λ, traveling in a medium with refractive index n. The diffraction also puts a lower bound on the core dimension of optical fibers and optical waveguides, making the optical devices and interconnects much large in comparison to the integrated electrical counterpart. While light matter interaction at nano-scale provides insight on fundamental phenomenon, from study of biological processes to interatomic transition, the diffraction limit has hampered the scientific community to venture into these studies. In turn, we had to resort to non-optical methods like electron microscopy and fluorescence microscopy.

Plasmonics forms an emerging field of nanophotonics that allows electromagnetic fields to be confined to dimensions smaller than the wavelength. It is a result of coupling of light to free electrons in metals at the metal-dielectric interface leading to enhanced optical near-fields (resonance amplification). Surface Plasmons Polaritons (SPPs) are highly confined, non-radiating propagating waves on the surface of a conductor, where the fields decay exponentially in direction normal to the surface (Fig.1.1(a)). However due to momentum mismatch, incident light cannot directly couple to the plasmons, hence structures such as prism, grating and tapered waveguide etc. are used to achieve the coupling. Since surface plasmons occur at the metal-dielectric interface, these charge density oscillations when confined to a metal nanoparticle are called Localized Surface Plasmons (LSPs), as depicted in Fig.1.1(b). The LSPs resemble a dipole with charges localized at the two poles. When the nanoparticle is small compared to the wavelength, it can be approximated as point dipole. As

the incident electromagnetic wave oscillates, the poles oscillate at the same frequency.

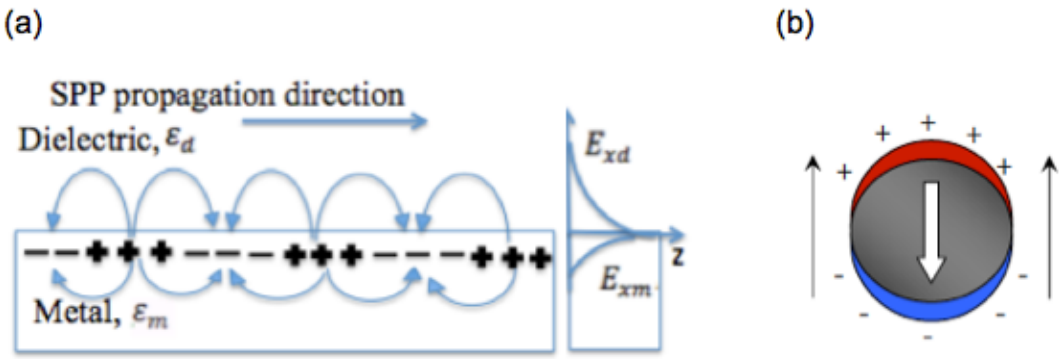

Fig.1.1: Schematic showing surface plasmon oscillations on (a) planar metal-dielectric interface and (b) metallic nanoparticle induced by electromagnetic fields showing the fundamental LSP mode. The fields in metal and dielectric decay exponentially from the interface, depending upon the permittivity of metal, ε_m and the dielectric, ε_d .

Sommerfeld and Zenneck provided the initial formulation of surface waves where radio waves traveled along the surface the earth, or a conductor with finite conductivity [1]. The phenomenon of surface waves in the visible domain was first reported by R. W. Woods in 1902, when he observed narrow-bands in the diffraction spectrum of metal-grating due to coupling of some part of incident light to the metal surface; commonly referred to as the Woods' anomaly [2]. Later much of the pioneering work describing surface plasmons was carried out by Richtie *et al.* [3], where they studied diffraction of electron beams from thin metallic foils due to interactions at the metal interface which was later expanded to the study on diffraction gratings [4]. Although surface plasmons have been studied recently, the property of metallic structures to couple light has been known for centuries, dating back to the 4th century A.D. where Lycurgus cup (Fig.1.2) made of dichroic glass appears red when lit from inside and green when illuminated from the outside. The dichroic effect was achieved due to presence of gold nanoparticles, which exhibits surface plasmon resonance producing

this exciting effect.

Fig.1.2: Lycurgus Cup, the 4th century Roman glass cage cup, made of glass with colloidal sub-100 nm gold nanoparticles. The glass appears green when illuminated from outside and bright red when light is passed from inside.

Despite the observation of surface plasmons - SPPs and LSPs in the early 20th century, the field of plasmonics did not gain much attention until mid 1970's with the observation of enhanced scattering by roughened silver surface with active Raman molecules, leading to discovery of Surface Enhanced Raman Spectroscopy (SERS). The technology is today widely used in sensing biological and chemical molecules. Later in 1997, with observation of extraordinary transmission of light through metallic hole-arrays by Ebbeson *et al.* [4], re-invigorated the interest in the field, leading to a flurry of papers and applications [5]. Later the concept was expanded to beam forming through bulls-eye structure [6], periodic and aperiodic hole arrays in visible as well as THz frequency regime [7-9]. Different waveguide structures for surface plasmons have also been explored recently, based on nano-wires and complementary metal-insulator-metal waveguides [10-12].

Our work is inspired by recently proposed Resonant Guided Wave Networks (RGWNs), by E. Feigenbaum *et al.* [13], where color routers were proposed based on intersecting plasmon waveguides. In the work scattering matrix was developed for the network that was

optimized for operation as a color router. In this work, we proceed with study of the behavior of plasmon waveguides and simple waveguide components and L-, T- bends and 4-port splitter formed intersection of two plasmon waveguides at optical frequencies. We study the reflection and transmission characteristics of these structures using Finite Difference Time Domain (FDTD) simulations. Later we realize different directional devices, like color router and filters based on 2 X 2 waveguide network.

1.1 Motivation

With Moore's law approaching its limits, silicon photonics is seen as the next big thing. The increasing demand from data centers and our move towards next generation technologies, like artificial intelligence and machine learning, require manifold increase in information processing capabilities at a much faster rate. The concept behind photonics is simple, i.e., it utilizes light, the fastest known phenomenon, but it comes with a drawback and deviates from the well-established Moore's law. As discussed above the confinement of light is limited by the diffraction limit. The optoelectronic devices that are available today are much bigger in size when compared to semiconductor based electronic devices. Achieving technologies down to sub-wavelength scale requires control of light-matter interaction at nano-scale, where Plasmonics appears as promising candidate. Plasmonics provide unique capability to guide and manipulate light in sub-wavelength structures and provide true counterpart to electronic devices. Fig.1.3 aptly describes the advantage of plasmonics over photonics and electronics as promising technologies to tackle the future challenges. The light confinement in metal-insulator-metal (MIM) plasmonic waveguides allows propagation of waves at wavelength much shorter than that in free space. The intersection of waveguides acts as a power-splitting element. As the wave also gathers phase during the propagation, the interference and resonance effects can be engineered by varying the geometry of the structure while the amplitude of power into each waveguide, at the power splitting element, can be controlled by

the width of the insulator. The structures based on these waveguides are being explored for integrated active and passive nanophotonic devices. Along with providing faster and smaller devices for information processing, owing to unique properties of surface plasmons, it offers many opportunities in the field of medicine and quantum studies, among others. The high field confinement and enhancement due to resonance effects has enabled highly efficient bio- and chemical sensing down to single molecule detection. Due to large Photonic Density of States (PDOS), it can also be utilized for fluorescence decay studies and high quality factor (Q-factor) resonator based devices for spontaneous decay enhancement of Quantum Dot. Other emerging technologies based of plasmonics include highly efficient displays, nano-antenna, and Anderson localization of light and Electromagnetically Induced Transparency (EIT) due to Fano resonance.

In this thesis, we explore the theory and properties of surface plasmons in planar structures. We investigate the dispersion relations of multilayer metal-dielectric waveguide and derive relations for the two lowest order bound TM modes, referred to as the symmetric and asymmetric modes. We also discuss the emerging technologies based on plasmonics and extraordinary properties that have opened up many novel potential applications. In particular, we investigate the surface plasmon guided-wave devices that utilize interference effects within multiple intersecting MIM waveguides. These waveguides are composed of $Ag/SiO_2/Ag$ and the specific devices we have explored include guided-wave devices such as the L and T-bends, 4-way splitters and 2x2 networked structures wherein by altering the device geometry, one can tune its operating frequency, and by changing the angle of incidence one can switch these devices between on and off states. The results have been established using FDTD simulations and the devices are fabricated by focused-ion milling into thin film deposited metal-insulator layers on a silica substrate, where the milled-structures are filled with index matching fluid. The devices are characterized using

transmission spectroscopy technique.

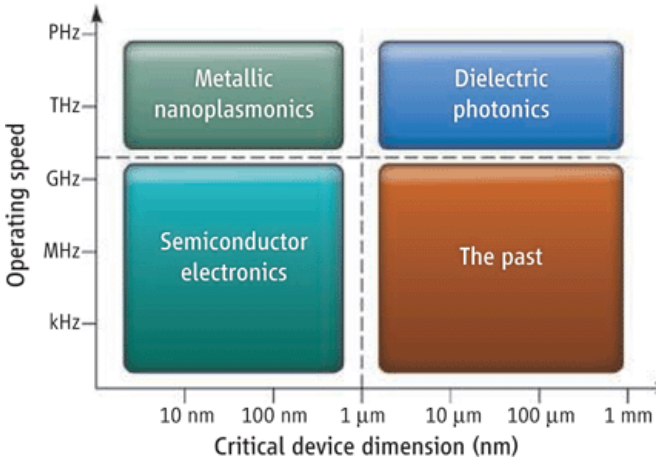

Fig.1.3: Schematic depiction of comparison of feature size and operating speeds for plasmonics based technology vs. dielectric-based photonic devices, and semiconductor electronics [14].

1.2 Scope of the Thesis

In this thesis, an effort has been made to provide the basic theory behind the field of Plasmonics. In Chapter 2, we discuss the properties of metals with finite conductivity that supports these surface plasmons. The relations for plasmon frequency and critical conditions for bound surface modes have been discussed. In Chapter 3, we derive the dispersion relation for the plasmon at single metal-dielectric surface. Later different waveguide structures comprising of dielectric-metal-dielectric layer and the complementary structures have been studied. Chapter 4 covers the techniques adopted to excite and image surface plasmons and the phenomenon of plasmon excitation of metal nanoparticles. After discussing the fundamentals and properties of surface plasmons, in Chapter 5, we present our work on guided-wave devices based on MIM geometry and the FDTD simulation results of different waveguide components and basic design rules to be considered while designing such devices. Finally we present devices such as directional color router and filter configuration based on

2 X 2 waveguide structures. We also discuss the device fabrication process, experiment setup to be followed as the future work. The numerical techniques used to realize plasmonic devices are also discussed in brief. We then conclude the thesis with the discussion of results and prospects of future work.

2 Electromagnetic Modes in Metals

One of the widely accepted theories in solid-state, Drude model for free electrons, describes the properties of metals using the concept of plasma. According to the Drude's model, valence electrons in metals move around the fixed ions in the lattice of the metal. In the simplest form it assumes that the interaction between the electrons is neglected and the electrons are free to move through the lattice. Although Drude's model, being classical in nature, interestingly describes the electrical properties of metals in good conjunction with the experiments, the model fails to capture the thermal properties like specific heat and thermal conductivities completely. The model was later modified by Sommerfeld to include the effect of quantum oscillations and was later challenged by Fermi that states the Fermi-Dirac distribution of electrons around the nucleus, considering Pauli's exclusion principle and the quantization of electron levels [15]. Here we focus on Drude's model to describe electrical and optical properties of material relevant and adequate to explain the fundamentals of plasmonics. We can describe the optical properties of metals using classical mechanics even for metallic nanostructures due to high density of electrons, which provides a small band-gap as compared to K_BT at room temperature, where K_B is the Boltzmann's constant. We approach the explanation of electromagnetics in metals beginning from Maxwell's equations.

2.1 Metals and Electromagnetics Waves

Metals are highly reflective for frequencies below visible part of the spectrum and hence, are employed as cladding material for waveguides in microwave and infrared regime. In this regime the approximation of metal being a perfect conductor is valid, since the fields penetrate very small distances into the metal, termed as the skin depth. However, when we go to higher frequencies, towards the visible regime, this penetration of fields increases significantly. This results in increased dissipation of energy, thus restricting the metal

structures to be used for optical and photonic devices, and hence we resort to dielectrics for propagation. When we go further high towards the bulk plasma frequency, metals become transparent, i.e., they behave like dielectric and allow propagation of EM waves, the phenomenon termed as Ultraviolet Transparency [15].

The above mentioned properties of metals can be easily explained by frequency dependent complex permittivity, $\varepsilon(\omega)$. One of the explanations for this dispersive property of permittivity function proposes that the phase of the induced currents for driving field changes at different frequencies. Using the constitutive relations:

$$\mathbf{D} = \varepsilon_0 \mathbf{E} + \mathbf{P} = \varepsilon_0 \varepsilon \mathbf{E} \tag{2.1a}$$

$$\mathbf{B} = \mu_0 \mathbf{H} + \mu_0 \mathbf{M} = \mu_0 \mu \mathbf{H} \tag{2.1b}$$

where, ε_0 and μ_0 are permittivity and permeability of free space, and ε and μ are relative permittivity and permeability of the material. One more constitutive relation important in this context, relates current density **J** and **E** by a linear relation, i.e.

$$\mathbf{J} = \frac{ne^2 \boldsymbol{E}\tau}{m_e}, \tag{2.2}$$

which gives the microscopic form of Ohm's law ($\mathbf{J} = \sigma \boldsymbol{E}$)**.** Here τ is the relaxation time between two scattering events by an electron, e is charge of an electron and m_e denotes its mass. Electrons in Drude model move freely in the lattice of fixed ions, for a material with net charge of zero. These electrons scatter randomly while conserving the total energy. When the electric field is applied across the metals, the electrons are subject to a force equal to $e\boldsymbol{E}$ and gain a net momentum of $e\boldsymbol{E}\,\tau$, as shown in Fig.2.1. Thus using $\mathbf{J} = -ne\nu$ gives equation (2.2), where ν is the net velocity gained by the electrons and n is the number of free/conduction

electrons. This provides an approximation to behavior of metals to static electric field.

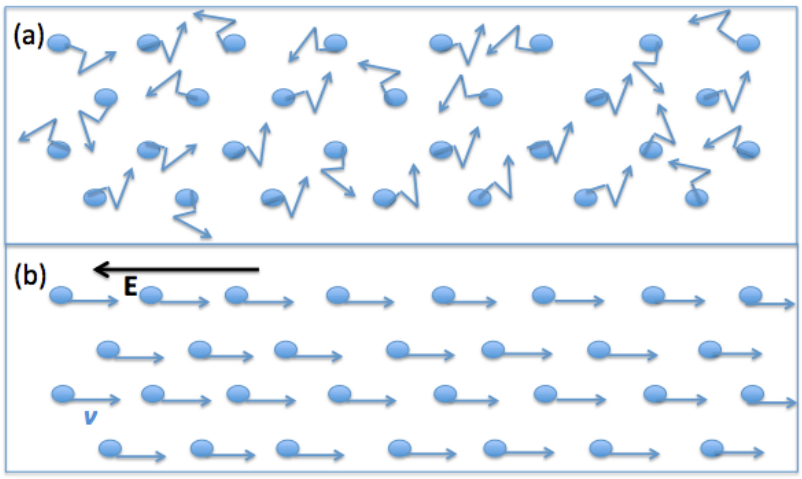

Fig.2.1 Schematic for Drude model of free electron gas where electrons move in random manner. When the metal is subjected to static electric field, electrons gain a net velocity in the direction opposite to that of the field.

We also take into account that the optical response of metals depends upon the frequency. Thus equation (2.1) and Ohm's law in Fourier domain (taking the spatially local response) are modified to:

$$\mathbf{D}\,(\omega) = \varepsilon_0 \varepsilon(\omega)\mathbf{E}(\omega), \tag{2.3a}$$

$$\mathbf{J}\,(\omega) = \sigma(\omega)\mathbf{E}(\omega) \tag{2.3b}$$

Also, using the relation $\nabla.\mathbf{P} = -\rho$, and substituting in continuity equation we get:

$$\mathbf{J} = \frac{\partial \mathbf{P}}{\partial t} \tag{2.4}$$

Now, substituting the values in Maxwell's equations:

$$\nabla.\boldsymbol{E} = 0$$

$$\nabla . \boldsymbol{H} = 0$$

$$\nabla \times \boldsymbol{E} = -\frac{\partial \boldsymbol{B}}{\partial t}$$

$$\nabla \times \boldsymbol{H} = \sigma \boldsymbol{E} + \varepsilon \varepsilon_0 \frac{\partial \boldsymbol{E}}{\partial t} \tag{2.5}$$

We obtain dispersive property of permittivity,

$$\varepsilon(\omega) = 1 + \frac{i\sigma(\omega)}{\varepsilon_0 \omega} \tag{2.6}$$

At low frequencies, ε reflects the contribution of bound charges and σ the contribution of free charges.

2.2 Damped Oscillator Model – Plasma model

Since the electron gas is confined in three dimensions, the displacement of electrons with respect to lattice fixed positive nucleus leads to a restoring force. Thus the electrons subjected to an electric field can be approximated by a damped oscillator model [15]. For a dispersive media the force equation is given by:

$$-e\boldsymbol{E} = m_e \left(\frac{\partial^2 \boldsymbol{r}}{\partial t^2} + \gamma \frac{\partial \boldsymbol{r}}{\partial t} + {\omega_0}^2 \boldsymbol{r} \right), \tag{2.7}$$

where γ is the damping coefficient and ω_o is the resonant frequency and $\mathbf{r}(t) = \mathbf{r}e^{-i\omega t}$ describes the oscillation of electrons. From (2.7), the displacement **r** takes the form:

$$\boldsymbol{r} = \frac{e}{m_e(\omega^2 - {\omega_0}^2 + i\gamma\omega)} \boldsymbol{E} \tag{2.8}$$

Thus displacement of electrons with the oscillating field leads to polarization, $\boldsymbol{P} = -ne\boldsymbol{r}$

$$\boldsymbol{P} = \frac{-ne^2}{m_e(\omega^2 - {\omega_0}^2 + i\gamma\omega)}\boldsymbol{E} \tag{2.9}$$

For source free Maxwell's equation, Ampere's Law is given by:

$$\nabla \text{ x } \mathbf{H} = -\text{i}\omega(\varepsilon_0 \mathbf{E} + \mathbf{P}) = -\text{i}\omega\, \varepsilon_0 \varepsilon_\text{m}\, \mathbf{E} \tag{2.10}$$

Thus we obtain $\varepsilon_\text{m}(\omega) = \left(1 - \frac{{\omega_p}^2}{\omega^2 - {\omega_0}^2 + i\gamma\omega}\right)$,

where ω_p is the plasma frequency of free electron gas given by the relation:

$${\omega_p}^2 = \frac{ne^2}{m_e \varepsilon_0}$$

For conductors (metals): $\varepsilon_\text{m}(\omega) = \left(1 - \frac{{\omega_p}^2}{\omega^2 + i\gamma\omega}\right) = \varepsilon'(\omega) + \varepsilon''(\omega)$ (2.11)

This gives us the AC equivalent of Ohm's law, $\boldsymbol{D} = \varepsilon_0 \left(1 - \frac{{\omega_p}^2}{\omega^2 + i\gamma\omega}\right) . \mathbf{E}$

Separating the real and imaginary parts of relative permittivity, and using $1/\gamma = \tau$ we get,

$$\varepsilon'(\omega) = \left(1 - \frac{{\omega_p}^2 \tau^2}{\omega^2 \tau^2 + 1}\right) \tag{2.12a}$$

$$\varepsilon''(\omega) = \left(\frac{{\omega_p}^2 \tau}{\omega(\omega^2 \tau^2 + 1)}\right) \tag{2.12b}$$

Now considering the case of very high frequencies, i.e. for $\omega \gg \omega_p$, $\varepsilon'(\omega)$ is close to 1, and $\varepsilon''(\omega)$ approaches zero, thus, the metals become transparent, hence behave as dielectric, while for $\omega < \omega_p$, they retain their electric character and are highly reflective. For the frequencies close to the plasma frequency, the imaginary part approaches zero, thus the effect of damping is negligible and the permittivity takes the predominantly real form.

$$\varepsilon(\omega) = \left(1 - \frac{{\omega_p}^2}{\omega^2}\right) \tag{2.13}$$

Johnson and Christy [16] measured the real and imaginary parts of refractive index n' and n'', for different metals using ellipsometric technique, the real and imaginary values of permittivity can be obtained from these values by the relation:

$$\varepsilon'(\omega) = {n'}^2 - {n''}^2, \tag{2.14b}$$

$$\varepsilon''(\omega) = 2n'n'' \tag{2.14b}$$

From the results obtained by the measurement, it was observed that the metals possess high negative real values for permittivity as shown for the case of silver, Ag, in Fig.2.2.

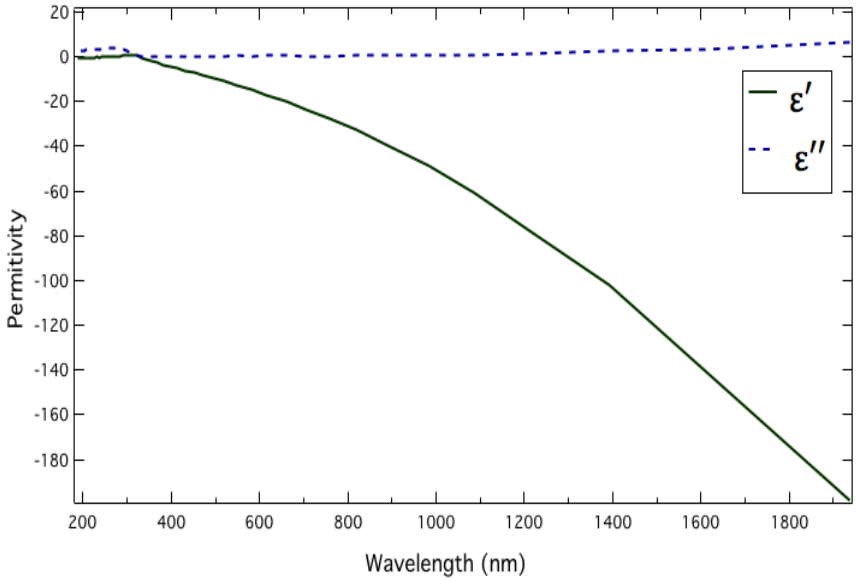

Fig.2.2: Real and imaginary values of permittivity for Silver, obtained from data recorded by Johnson and Christy [15].

2.3 Volume/ Bulk Plasmons

Since we know from the dispersion relation: the propagation constant $\boldsymbol{k}$ is related by:

$$\boldsymbol{k^2} = \varepsilon(\omega)\frac{\omega^2}{c^2}$$

$$\boldsymbol{k^2} = \left(1 - \frac{{\omega_p}^2}{\omega^2}\right)\frac{\omega^2}{c^2} \qquad (2.15)$$

For $\omega < \omega_p$, $\boldsymbol{k}$ becomes imaginary, thus the transverse wave cannot propagate inside the metal, and the wave attenuates into the metal. For $\omega > \omega_p$,

$$\omega^2 = {\square_p}^2 + \boldsymbol{k^2}c^2$$

Thus the transverse wave travels inside the metal though the metal plasma, called the volume plasmons as shown in Fig.2.3.

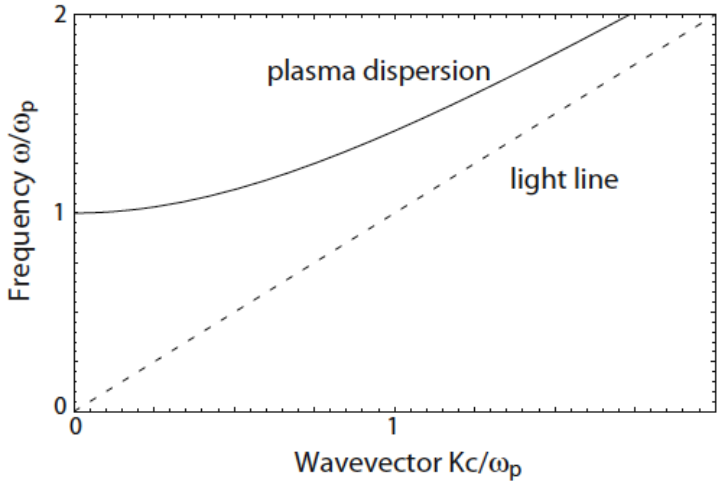

Fig.2.3: Dispersion relation of volume plasmons [17]

At $\omega = \omega_p$ (plasma frequency), $\varepsilon(\omega) = 0$, thus the displacement,

$$\boldsymbol{D} = \varepsilon_0\varepsilon(\omega_p)\boldsymbol{E} = 0.$$

$$\boldsymbol{E} = -\frac{\boldsymbol{P}}{\varepsilon_0}$$

Thus at plasma frequency, a longitudinal wave travels along the metal surface.

3 Surface Plasmon Polaritons in Planar Structures

Surface Plasmon Polaritons are hybrid photon-electron modes that propagate along the surface of a conductor. These waves are light waves trapped on the interface due to its interaction with the free electrons [18] and are highly lossy due to Ohmic losses in metals. One of the major challenges is to concentrate light and channel them efficiently into sub-wavelength structures. In this chapter we discuss the properties of SPP at single metal-dielectric interface as well as in planar waveguide structures.

3.1 SPP at Metal-Dielectric Interface

We begin our analysis with the wave equation obtained from Maxwell's equations that gives propagation of fields in media with complex relative permittivity ε, with wave vector, k_0 in free-space :

$$\nabla^2 \boldsymbol{E} = \frac{\varepsilon}{c^2}\frac{\partial^2 \boldsymbol{E}}{\partial t^2} \quad or \quad \nabla^2 \boldsymbol{E} + k_0^2 \varepsilon \boldsymbol{E} = \boldsymbol{0} \tag{3.1}$$

For simplicity we consider the case of one dimensional planar waveguide geometry, where the wave is propagating in x direction, as shown in the schematic in Fig.3.1.

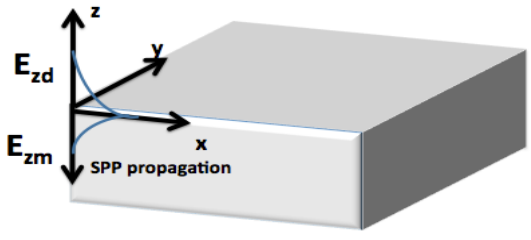

Fig.3.1: Schematic showing one-dimension problem for SPP propagation at metal-dielectric interface at z=0. $\boldsymbol{E_{zm}}$ and $\boldsymbol{E_{zd}}$ represent the penetration of E field inside the metal and dielectric respectively.

For the TM wave incident on the surface, the electric field takes the form:

$$\boldsymbol{E}(x,z,t) = \boldsymbol{E_0} e^{i(k_x x - k_z|z|)} \tag{3.2}$$

Separating the components of curl equations for electric and magnetic fields and substituting harmonic time-dependence, $\frac{\partial}{\partial t} = -i\omega$, we get the following six equations:

$$\frac{\partial E_z}{\partial y} - \frac{\partial E_y}{\partial z} = i\omega\mu_0 H_x, \tag{3.3a}$$

$$\frac{\partial E_x}{\partial z} - \frac{\partial E_z}{\partial x} = i\omega\mu_0 H_y, \tag{3.3b}$$

$$\frac{\partial E_y}{\partial x} - \frac{\partial E_x}{\partial y} = i\omega\mu_0 H_z, \tag{3.3c}$$

$$\frac{\partial H_z}{\partial y} - \frac{\partial H_y}{\partial z} = -i\omega\varepsilon_0\varepsilon E_x, \tag{3.3d}$$

$$\frac{\partial H_x}{\partial z} - \frac{\partial H_z}{\partial x} = -i\omega\varepsilon_0\varepsilon E_y, \tag{3.3e}$$

$$\frac{\partial H_y}{\partial x} - \frac{\partial H_x}{\partial y} = -i\omega\varepsilon_0\varepsilon E_z \tag{3.3f}$$

Assuming an infinite plane in y-direction, $\frac{\partial}{\partial y} = 0$, and using $\frac{\partial}{\partial x} = ik_x$, we get:

$$\frac{\partial E_y}{\partial z} = i\omega\mu_0 H_x \;\; or \;\; H_x = -i\frac{1}{\omega\mu_0}\frac{\partial E_y}{\partial z} \tag{3.4a}$$

$$\frac{\partial E_y}{\partial z} - ik_x E_z = i\omega\mu_0 H_y, \tag{3.4b}$$

$$ik_x E_y = i\omega\mu_0 H_z \quad \text{or} \quad H_z = \frac{k_x}{\omega\mu_0} E_y \tag{3.4c}$$

$$\frac{\partial H_y}{\partial z} = i\omega\varepsilon_0\varepsilon E_x \; or \; E_x = -i\frac{1}{\omega\varepsilon_0\varepsilon}\frac{\partial H_y}{\partial z} \tag{3.4d}$$

$$\frac{\partial H_y}{\partial z} - ik_z H_z = -i\omega\varepsilon_0\varepsilon E_x \tag{3.4e}$$

$$ik_x H_y = -i\omega\varepsilon_0\varepsilon E_z \; or \;\; E_z = -\frac{k_x}{\omega\varepsilon_0\varepsilon}H_y \tag{3.4f}$$

Thus for TM wave solution $E_z, E_x, H_y \neq 0$, and $E_y = H_z = H_x = 0$. Alternatively for TE wave solution, we have $E_y, H_x, H_z \neq 0$, and $E_x = E_z = H_y = 0$.

Now defining the ***E*** fields, for TM waves for the two regions metal (m) and dielectric (d):

$$\boldsymbol{H_{dy}} = \; Ae^{i(k_{dx}x - k_{dz}|z|)} \tag{3.5a}$$

$$\boldsymbol{E_{dx}} = \; i\frac{A}{\omega\varepsilon_0\varepsilon_d}e^{i(k_{dx}x - k_{dz}|z|)} \tag{3.5b}$$

$$\boldsymbol{E_{dz}} = \; A\;\frac{k_x}{\omega\varepsilon_0\varepsilon}e^{i(k_{dx}x - k_{dz}|z|)} \tag{3.5c}$$

From eq. (3.4d): $$ik_{dz}H_{dy} = i\omega\varepsilon_0\varepsilon_d E_{dx}, \tag{3.6a}$$

$$ik_{mz}H_{dy} = i\omega\varepsilon_0\varepsilon_m E_{mx}, \tag{3.6b}$$

Using the boundary conditions, ensuring continuity of tangential components of electric and magnetic fields, i.e.

$$H_{dy} = \; H_{my} \;\; and \;\; E_{dx} = E_{mx} \tag{3.7a}$$

we obtain $$\frac{k_{mz}}{\varepsilon_m} = \frac{k_{dz}}{\varepsilon_d} \tag{3.7b}$$

Also $$k_{mx} = k_{dx} \equiv k_x$$

Using the dispersion relation :

$$k_x{}^2 + k_{iz}{}^2 = \varepsilon_i \left(\frac{\omega}{c}\right)^2 \tag{3.8}$$

where i =m,d. $$k_x = \sqrt{\varepsilon_i \left(\frac{\omega}{c}\right)^2 - k_{iz}{}^2} \tag{3.9}$$

From eqs. (3.7) and (3.9), we get the most important relation for our thesis, the dispersion relation for surface plasmon, given by:

$$k_x = \frac{\omega}{c}\sqrt{\frac{\varepsilon_d \varepsilon_m}{\varepsilon_d + \varepsilon_m}} \tag{3.10}$$

From dispersive properties of permitivity plotted in chapter 2, we know $\varepsilon_m' \gg \varepsilon_m''$ for higher frequncies for metals (Ag in our case). Thus separating the real and imaginary part of k_x which can be represented as $k_x = k_x' + ik_x''$, we get [18]

$$k_x' = \frac{\omega}{c}\sqrt{\frac{\varepsilon_d \varepsilon_m'}{\varepsilon_d + \varepsilon_m'}}, \tag{3.11a}$$

$$k_x'' = \frac{\omega}{c}\left(\frac{\varepsilon_d \varepsilon_m'}{\varepsilon_d + \varepsilon_m'}\right)^{3/2} \frac{\varepsilon_m''}{2\varepsilon_m} \tag{3.11b}$$

Case 1: From eq (3.10), the frequency at which $\varepsilon_m = -\varepsilon_d$, the real part of wave vector k_x' approaches infinity. *This frequency is called surface plasmon frequency, denoted by* ω_{sp}. Thus SPP approaches a finite maximum wave vector $\mathbf{k_{sp}}$.

Case 2: For low frequencies $\varepsilon_m \to \infty$, thus the eq (3.10) reduces to $k_x = \frac{\omega}{c}\sqrt{\varepsilon_d}$, thus approaching the light line

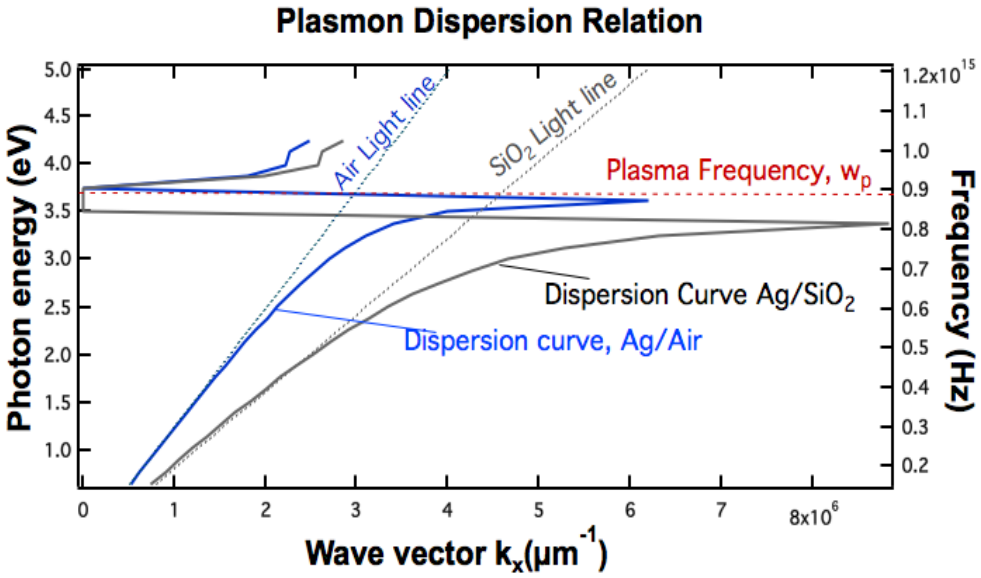

Fig.3.2: Dispersion relation for SPP at metal- dielectric interface. The dotted blue line represents the dispersion curve for propagation in free space, the blue line represents the dispersion curve for metal-air interface. Corresponding grey curves represent the dispersion curves for Ag-SiO_2 interface.

As the propagation of SPP decay as $e^{-k_x'' x}$. Thus the propagation length of the surface plasmon wave is given by : $L = (2k_x'')^{-1}$.

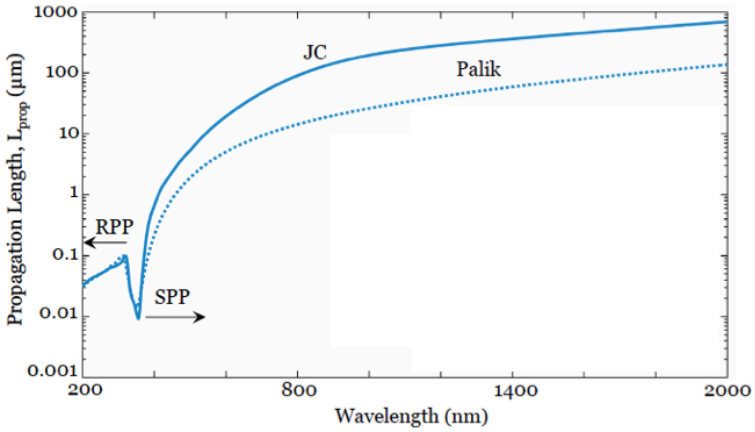

Fig.3.3: Propagation Length of surface plasmon at Ag/SiO_2 interface for permittivity data from Johnson and Christy (JC) and Palik. RPP represents the radiative plasmon

polaritons than propagate through the metal above the plasma frequency (Plot obtained from ref [21])

We now analyze TE mode solutions:

$$E_{dy} = Ce^{i(k_{dx}x - k_{dz}|z|)} \tag{3.12a}$$

$$H_{dx} = i\frac{C}{\omega\mu_0}e^{i(k_{dx}x - k_{dz}|z|)} \tag{3.12b}$$

$$H_{dz} = C\frac{k_x}{\omega\mu_0}e^{i(k_{dx}x - k_{dz}|z|)} \tag{3.12c}$$

$$E_{my} = De^{i(k_{mx}x - k_{mz}|z|)} \tag{3.12d}$$

$$H_{mx} = i\frac{D}{\omega\mu_0}e^{i(k_{mx}x - k_{mz}|z|)} \tag{3.12e}$$

$$H_{mz} = C\frac{k_x}{\omega\mu_0}e^{i(k_{mx}x - k_{mz}|z|)} \tag{3.12f}$$

Similarly, from the boundary conditions, we ensure continuity of the tangential **E** and **H** fields. We get $C(k_{dz} + k_{mz}) = 0$. Since $\mathbb{R}(k_{dz}) > 0$ and $\mathbb{R}(k_{mz}) > 0$ for surface confinement, thus $C = D = 0$. *Thus, only TM polarized modes exist and propagate along the surface.*

Before moving on to the next section we investigate the the field confinement at the interface. We know from the dispersion relation eq (3.9):

$$k_z = \sqrt{\varepsilon_i\left(\frac{\omega}{c}\right)^2 - {k_x}^2}$$

From the dispersion curve (Fig.3.3) we see that k_x is always greater than free space propagation vector for surface plasmon wave, thus the wave vector in z direction is imaginary. Hence we know that the fields decay as $e^{-k_z'' z}$ normal to the surface. We also see that SPP near ω_{sp} has high field confinement. Also at these high frequencies the propagation length is small due to increased damping. Thus increased confinement is achieved at a cost of short propagation length.

3.2 Coupled Surface Plasmon Polaritons

We now consider the SPP in multilayer planar structures composed of alternating layers of metal and dielectric.

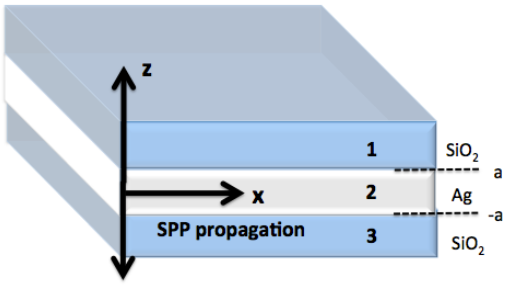

Fig.3.4: Schematic for dielectric-metal-dielectric waveguide.

We first consider the excitation by a TM polarized wave for dielectric-metal-dielectric (DMD) waveguide, shown in Fig. 3.4. The TM fields are given by:

Region 1: (Changing coefficients to D and $z \rightarrow -z$ for Region 3)

$$H_y^1 = Ce^{i(k_x x + k_{dz} z)} \tag{3.13a}$$

$$E_x^1 = iC\frac{1}{\omega\varepsilon_0\varepsilon_d}e^{i(k_x x + k_{dz} z)} \tag{3.13b}$$

$$E_z^1 = C\frac{k_x}{\omega\varepsilon_0\varepsilon_d}e^{i(k_x x + k_{dz} z)} \tag{3.13c}$$

Region 2:

$$H_y^2 = Ae^{i(k_x x - k_{mz} z)} + Be^{i(k_x x + k_{mz} z)} \tag{3.13d}$$

$$E_x^2 = -i\frac{1}{\omega\varepsilon_0\varepsilon_m}(Ae^{i(k_x x - k_{mz} z)} - Be^{i(k_x x + k_{mz} z)}) \tag{3.13e}$$

$$E_z^2 = \frac{k_x}{\omega\varepsilon_0\varepsilon_m}(Ae^{i(k_x x - k_{mz} z)} + Be^{i(k_x x + k_{mz} z)}) \tag{3.13f}$$

Inside the metal, the two surface waves at the interfaces z=a and z=-a. Solving the boundary conditions for continuity of H_y and E_x at interface z=a,-a, we get:

$$Ce^{k_{dz}a} = Ae^{-k_{mz}a} + Be^{k_{mz}a}, \quad and \quad De^{-k_{dz}a} = Ae^{k_{mz}a} + Be^{-k_{mz}a}$$

$$\frac{C}{\varepsilon_d}e^{k_{dz}a} = -\frac{A}{\varepsilon_m}e^{-k_{mz}a} + \frac{B}{\varepsilon_m}e^{k_{mz}a}, \quad and \quad -\frac{D}{\varepsilon_d}e^{-k_{dz}a} = -\frac{A}{\varepsilon_m}e^{k_{mz}a} + \frac{B}{\varepsilon_m}e^{-k_{mz}a}$$

Using the above four equations and the dispersion relations for the two media, we obtaing the following result for the two different modes:

$$\tanh k_{mz}a = -\frac{k_{dz}\varepsilon_m}{k_{mz}\varepsilon_d} \text{ (symmetric mode)} \tag{3.14a}$$

$$\coth k_{mz}a = -\frac{k_{dz}\varepsilon_m}{k_{mz}\varepsilon_d} \text{ (anti-symmetric mode)} \tag{3.14b}$$

Similarly for TM modes for metal-dielectric-metal (MDM) waveguide, shown in Fig. 3.5:

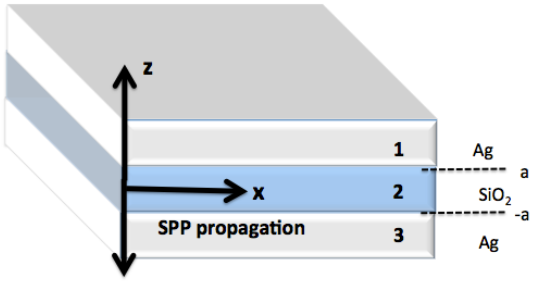

Fig.3.5: Schematic for metal-dielectric-metal waveguide

Region 1: (Changing coefficients to D and $z \rightarrow -z$ for Region 3)

$$H_y^1 = Ce^{i(k_x x + k_{mz} z)} \tag{3.15a}$$

$$E_x^1 = iC \frac{1}{\omega \varepsilon_0 \varepsilon_m} e^{i(k_x x + k_{mz} z)} \tag{3.15b}$$

$$E_z^1 = C \frac{k_x}{\omega \varepsilon_0 \varepsilon_m} e^{i(k_x x + k_{mz} z)} \tag{3.15c}$$

Region 2:

$$H_y^2 = Ae^{i(k_x x - k_{dz} z)} + Be^{i(k_x x + k_{dz} z)} \tag{3.15d}$$

$$E_x^2 = i \frac{1}{\omega \varepsilon_0 \varepsilon_m} (Ae^{i(k_x x - k_{dz} z)} + Be^{i(k_x x + k_{dz} z)}) \tag{3.15e}$$

$$E_z^2 = \frac{k_x}{\omega \varepsilon_0 \varepsilon_m} (Ae^{i(k_x x - k_{dz} z)} + Be^{i(k_x x + k_{dz} z)}) \tag{3.15f}$$

Similarly, solving these equations we obtain the complemetary result as eq (3.14)

$$\tanh k_{mz} a = -\frac{k_{mz} \varepsilon_d}{k_{dz} \varepsilon_m} \text{ (symmetric mode)} \tag{3.16a}$$

$$\coth k_{mz} a = -\frac{k_{mz} \varepsilon_d}{k_{dz} \varepsilon_m} \text{ (anti-symmetric mode)} \tag{3.16b}$$

3.3 Metal-Dielectric-Metal Waveguide

For the thin film (DMD) structures, the two solutions (3.14a), (3.14b) represent the symmetric (odd) for E_x and antisymmetric (even) funtions for H_y and E_z. For the antisymmetric modes, the confinement of fields inside the metal film is considerably less as compared to the symmetric modes, hence the mode is more confined in the dielectric material and attains plane wave behavior. These modes are called Long Range Surface Plasmon Polariton (LRSPP). The symmetric modes have more fields inside the metals which is highly lossy as compared to the dielectric. Similarly for MDM geometry two modes exist, as derived in eq. (3.16). Here the dominant mode is the symmetric mode and has no cut-off.

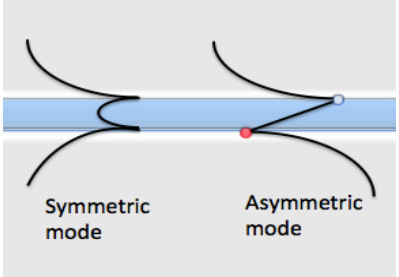

Fig.3.6: Schematic showing symmetric and antimmetric mode profile for MDM waveguide where the center layer of dielectric (blue) is sandwiched between the metal cladding (silver).

We can also solve for any arbitrary geometry of planar layered structures by solving the bounday conditons at each interface and using the dispersive properties for permittivity of metal layers. We limit ourselves here to discussion of symmetric modes in MDM waveguides.

These MDM structures have no cut-off for the fundamental mode and here the light can be squeezed to sub-nanometer dimension. The dispersion relation also depends on the width of the dielectric material and as the width is reduced, larger wavevectors are achieved as shown in Fig.3.7. The slope of the dispersion relation also gives the effective mode index. Thus the wave-vector of the SPPs can be engineered by varying the width of the dielectric waveguide. As the width of the waveguide is increased, the coupling between the SPPs at the two metal-dielectric decreases, as seen in the field profile for varying width given in Fig. 3.8. The group velocity, thus the effective mode index of the plasmon mode, can be obtained by calculating the slope of the curves in Fig. 3.7. The plots for effective mode index for different input wavelength are shown in Fig. 3.9.

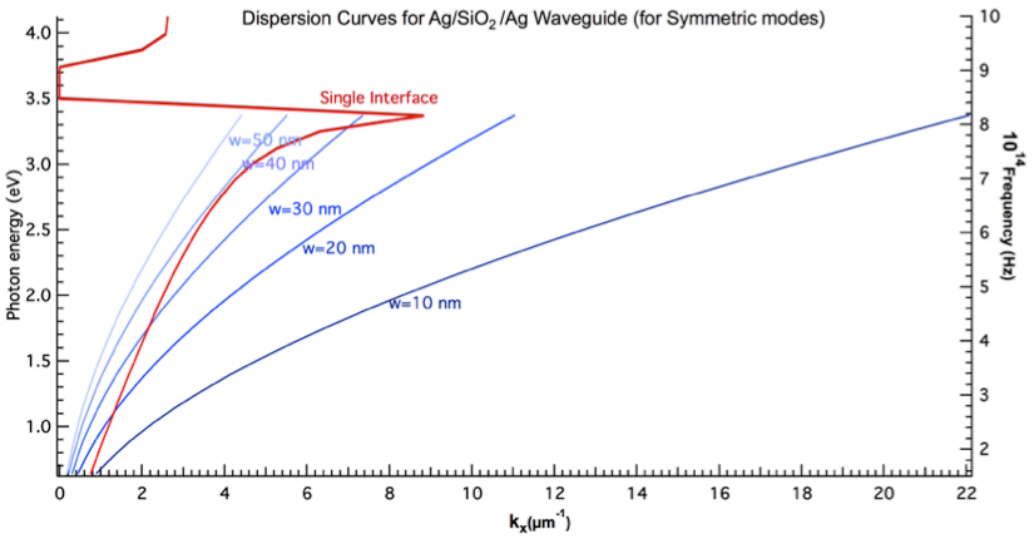

Fig.3.7: Dispersion relation for Ag-SiO_2-Ag waveguide for varying width, the results were eshatablised using the relation obtained by Economou *et al.*

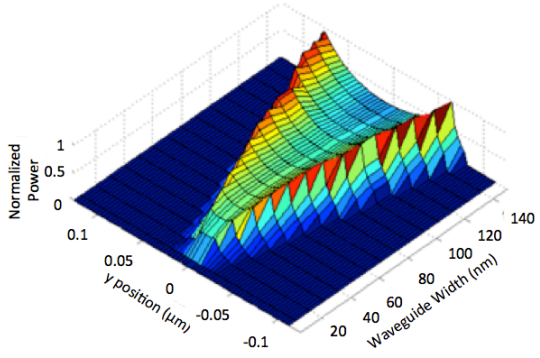

Fig.3.8: The figure shows the mode profile of the symmetric mode in Ag-SiO_2-Ag waveguide for different dielectric width. The results were obtained from FDTD simulation.

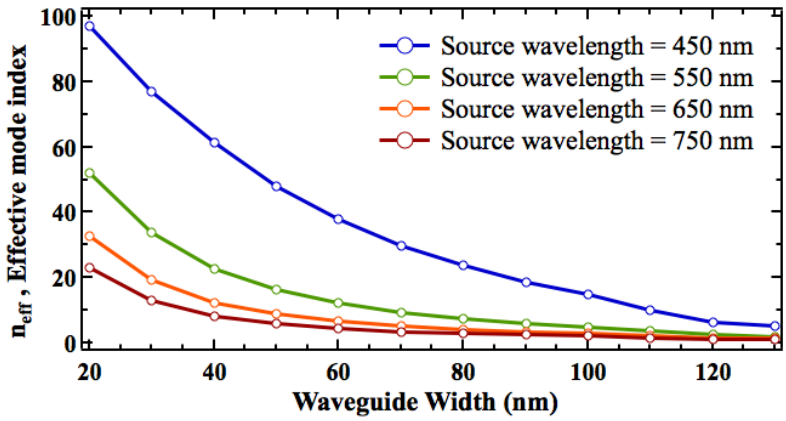

Fig.3.9: Effective mode index for MDM waveguide at different wavelength. The mode index is higher for small width of dielectric and the signal velocity is considerable reduced as the field is more confined into the metal. Also the mode showcases higher effective mode index as we approach the surface plasmon frequency.

It can also be seen from the Fig. 3.8, that the normalized field intensity is smaller for narrower waveguides as the amout of field confined in metal increases, leading to increased losses. Also from Fig.3.10, we see that the propagation length of SPP is smaller at the higher frequencies while the longer wavelengths support longer propagation length. This is attributed to the increased damping in metals at higher frequncies. Also the propagation length in MDM waveguide is determined by the width of the dielectric. For symmetric mode as the width is decreased the fields are more confined in the metal and attenuate more rapidly, hence decreasing the propagation length. Fig.3.11 below show the effect of wavelength and width on the propagation length. The knowledge of 1/e decay length can be useful in determining the optimal propagation length, hence defining the dimension of the devices. It can be seen that there exists a trade-off between the waveguide width and propagation length. The results were obtained through FDTD simulations.

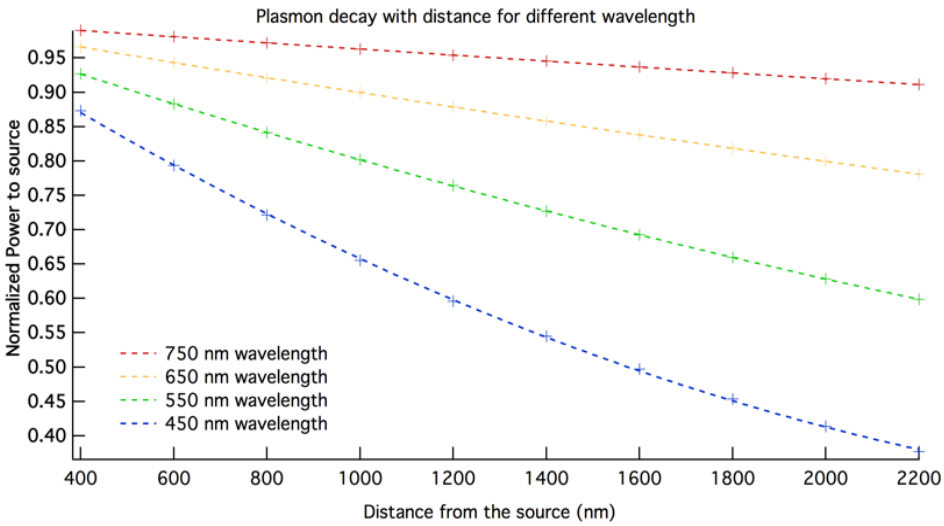

Fig.3.10: Plasmon decay with distance for different wavelength for Ag-SiO_2-Ag for dielectric width of 75nm

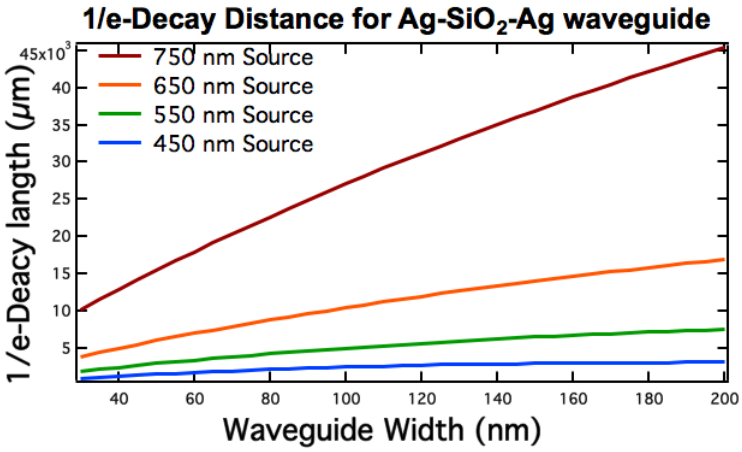

Fig.3.11: 1/e decay length for different wavelength and varying width of the waveguide.

In this chapter we studied the electromagnetic wave solutions in planar waveguide structures. We have established the basic properties of Ag-SiO_2-Ag plasmon waveguide. The results eshtablished through FDTD simulations provide us the optimum range of width and length to develop devices based on these waveguide structures.

4. Excitation and Imaging of Surface Plasmon Polaritons

In the previous chapter we have derived the electromagnetic wave solutions for the single interface and for multilayer structures. In this chapter we will discuss the widely used techniques and geometries used to excite the SPPs on the planar structures. We also discuss the common apparatus and methods used to image the surface plasmons and to determine the propagation lengths, field confinement (out-of plane fields) and intensity profile of the evanescent fields. We then discuss the phenomenon of plasmon scattering by the rough surface and the concept of Localized Surface Plasmon polaritons (LSPPs). In the end, we briefly analyze finite difference based numerical techniques to realize plasmonic structures.

4.1 Excitation of Surface Plasmon Polaritons on Planar Surfaces

From the dispersion relation derived in the previous chapter we see that the dispersion curve of the surface plasmon lies to the right of the free space propagation, thus the surface waves cannot be excited directly by shining light on the metal surface. In order to excite surface plasmon polaritons by TM polarized, two conditions must be met. Firstly, the frequency of the incident light must match the frequency of the SPP; secondly the component of wave-vector parallel to the metal surface must be equal to the wave vector of the SPPs. The first condition is inherently met, the wave vectors are matched by either photon tunneling or by using geometries/configurations which work on diffraction or total internal reflection. Different plasmon excitation geometries are shown in Fig. 4.1.

A. **Grating Coupler**

When the light is incident on the grating at an angle θ, its component in the direction parallel to the surface attains a wave-vector $(\omega/c)\sin\theta \pm ng$, where n is an integer and $g = 2\pi/a$ with a being the lattice spacing. Thus the extra momentum achieved using the gratings fulfills

the dispersion relation:

$$k_x = \frac{\omega}{c}\sqrt{\frac{\varepsilon_m}{1+\varepsilon_m}} = k_{sp} = \left(\frac{\omega}{c}\right)\sin\,\theta \pm ng \tag{4.1}$$

This can be generally written as

$$k_x = \left(\frac{\omega}{c}\right)\sin\theta \pm \Delta k_x$$

The resulting coupling to the surface can be observed as a dip in the frequency spectrum of the reflected light. These grating structures can also work as a decoupling device, i.e., a surface plasmon wave traveling along the grating discards the wave-vector component Δk_x and can propagate as a free wave.

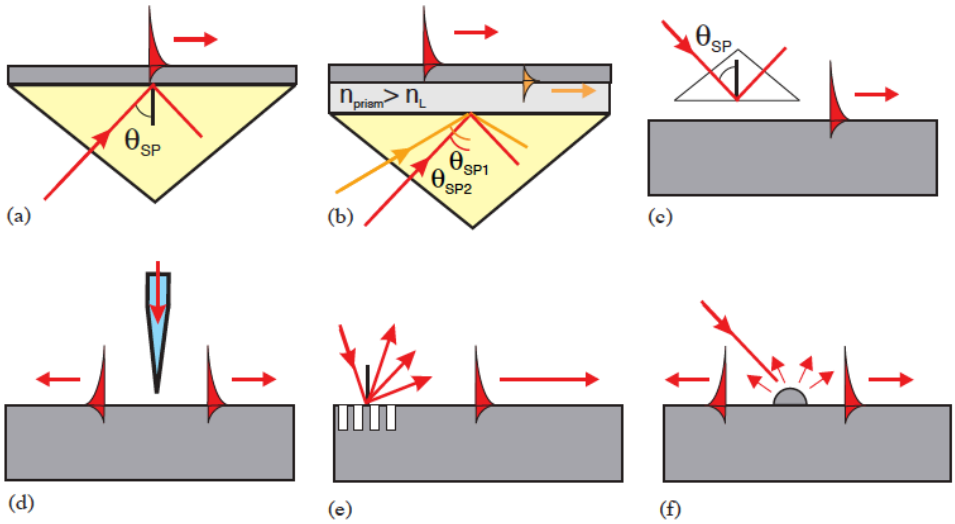

Fig. 4.1: Schematic showing different SPP excitation techniques (a) Kretschmann geometry, (b) two-layer Kretschmann geometry, (c) Otto geometry, (d) excitation with a SNOM probe, (e) diffraction on a grating, and (f) diffraction on surface features. (image taken from [23])

B. **Prism Coupling**

This technique utilizes the presence of evanescent wave extending into the surface at the point of total internal reflection. Different geometries have been proposed using prism as a dielectric medium on one side on the dielectric-metal-dielectric configuration. In the

Kretschmann geometry, a metal film placed on top of the dielectric is illuminated through the prism at the angle to incidence exceeding the critical angle causing the wave to undergo total internal reflection at the point of intersection where the evanescent wave tunnels through the metal film. The wave-vector of light being higher in the optically dense media provides the phase matching condition and the light is coupled to the surface plasmons:

$$k_x = \frac{\omega}{c}\sqrt{\varepsilon_{prism}}\sin\theta = k_{sp} \tag{4.2}$$

In order to excite surface plasmons on the inner surface of the metal, an additional dielectric is used between the prism and the metal where the refractive index *n* of the dielectric is less than that of the prism. In Kretschmann configuration as the metal thickness is increased, the tunneling through the metal is decreased and so is the intensity of surface plasmons. In case when the metal film is thick enough (or bulk metal) or when the Kretschmann configuration cannot be used, Otto configuration is used where the prism is placed close to the metal surface. When the total internal reflection occurs the photon tunneling occurs through the free space present between the prism and the metal surface. These SPPs are the leaky waves which lose energy by radiation into the prism along with the loss due to the absorption in the metal. In the case of prism coupling, a sharp minimum due to the destructive interference between the reflected and the radiated fields is observed in the reflection spectrum. The reflection coefficient using the Fresnel equation can be given by :

$$R = \left|\frac{E_r^{TM}}{E_0^{TM}}\right|^2 = \left|\frac{r_{pm}^{TM} + r_{md}^{TM} e^{i2k_z d}}{1 + r_{pm}^{TM} + r_{md}^{TM} e^{i2k_z d}}\right|^2, \tag{4.3}$$

where r_{12}^{TM} is the reflectivity at the interface given by :

$$r_{12}^{TM} = \frac{\left(\frac{k_{z1}}{\varepsilon_1} - \frac{k_{z2}}{\varepsilon_2}\right)}{\left(\frac{k_{z1}}{\varepsilon_1} + \frac{k_{z2}}{\varepsilon_2}\right)} \tag{4.4}$$

Using the Lorentzian approximation for the reflection coefficient given that the dielectric constant for metal satisfies $|\varepsilon'| \gg 1$ and $\varepsilon'' \ll \varepsilon'$, we obtain the reflection coefficient as:

$$R = 1 - \frac{4\Gamma_i \Gamma_{rad}}{\left(k_x - (k_x^0 + \Delta k_x)\right)^2 - (\Gamma_i + \Gamma_{rad})^2} \tag{4.5}$$

Here Γ_i and Γ_{rad} represent internal damping and radiation damping, where $\Gamma_i = Im(\Delta k_x)$, which depends upon the metal film thickness and $\Gamma_{rad} = Im(k_x^0)$. The reflection coefficient goes to zero when $\Gamma_i = \Gamma_{rad}$.

C. **Coupling Using Highly Focused Beams**

Another approach to couple the SPP using total internal reflection utilizes highly focused beam passing through a high numerical aperture objective lens illuminating the glass substrate as shown in Fig. 4.2. This excitation method allows for excitation in a diffraction limited spots, excitation for a continuum of frequencies as well as technique to subsequently determine the propagation lengths.

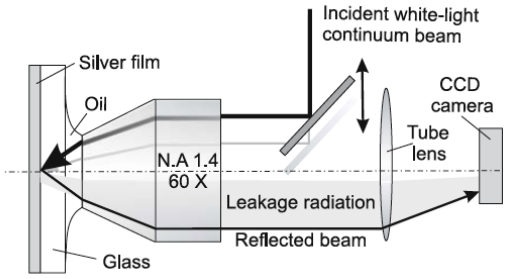

Fig. 4.2 : Schematic showing SPP excitation using a focused continuum light source [17].

Other SPP excitation techniques as shown in Fig. 4.1 (d),(f) include excitation using an near-field scanning optical microscopy (NSOM) tip, a tapered optical fiber which when brought sufficiently close to sample illuminates the metal surface with high k-vectors, matching the requirement for coupling. SPPs can also be excited by the random surface roughness. Here the near-field diffracted components of the light as scattered by the surface are coupled to the surface in the form of SPPs. The excitation due to random rough surface leads to low efficiency due to the non-resonant condition.

4.2 Imaging Surface Plasmon Polaritons: Near-field Scanning Optical Microscopy

Near-Field Scanning Optical Microscopy (NSOM or SNOM), shown in Fig. 4.3 is a scanning

probe technique used to image surface plasmons on the surface of the metal. NSOM also provides the technique used to excite SPP where an evanescent field from the tapered optical fiber tip that locally launches circular SPPs onto a metal surface.

As the SPPs propagate only a few microns, only scanning probe techniques could be applied to image surface plasmons. Earlier Scanning Tunneling Microscope (STM) technique was applied where presence of surface plasmon could be measured as an additional tunneling current produced due to interaction of surface charge oscillations with STM tip in the setup [17]. Other scanning probe techniques were used to detect surface plasmons, but it was later realized that such methods introduce perturbation effects caused by field enhancement due to LSPs. In NSOM technique a probe made up of optical fiber tip, which is tapered at the end, is used to scan the sample. The sharpened tip is usually made by pulling and tapering off the optical fiber in a controlled manner. The aperture of the optical fiber tip defines the resolution of the imaging technique. The refractive index of glass used in the sample is relatively small compared to the previous methods, thus minimizing the perturbation due to probing. The scanning probe technique allows detection of propagation length and the decaying tail of SPPs.

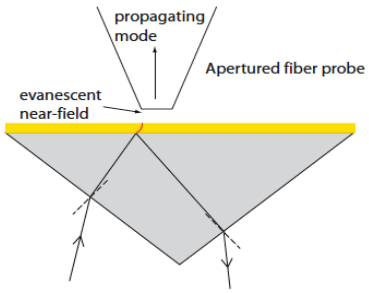

Fig. 4.3: Schematic for basic setup for Near-field Scanning Optical Microscopy. The techniques can also be used for excitation of surface plasmons by switching to the illumination mode through the optical fiber tip, where due to tapering of the fiber tip, the propagating mode turns evanescent and hence couples to the metal surface [17].

Imaging using Fluorescence technique: Another technique to image SPPs has emerged recently; it utilizes emitters like fluorescent molecules or quantum dots, which when placed in proximity to the surface plasmons absorbs the fields and in turn emit radiation. If the absorption band of the emitter covers the frequency of the surface plasmons, the emitters can be excited. Thus the emitted fluorescence radiation can be used to image SPPs while the intensity of radiation determines the strength of the fields [27]. The image can be used to study interference effects in surface plasmons in addition to field confinement and propagation lengths. The imaging resolution is limited by the diffraction limit defined by conventional optics.

4.3 Localized Surface Plasmons

After reviewing the properties of propagating surface plasmons on planar surface, here we discuss in brief about another type of surface plasmon oscillations in metallic nanostructures, which upon interaction with light results in Localized Surface Plasmons (LSPs). LSPs unlike SPPs are non-propagating plasmon modes which are generated on surface of these metallic structures due to oscillating fields. The modes in nanoparticles, due to the geometry and curvature exhibit resonance, result in field amplification both inside and in near field of these particles [17].

We discuss here the electromagnetic field solutions of isotropic metallic sphere of radius a *(*where $a << \lambda$*)* and frequency dependent dielectric constant $\varepsilon(\omega)$, placed at the origin surrounded by medium with dielectric constant ε_d , in the presence of uniform electric field (4.5)

$$\boldsymbol{E} = E_o \hat{z} = E_o r \cos\theta$$

The solution to the Laplace equation is $\nabla^2 \boldsymbol{\psi} = \mathbf{0}$, where the wave function $\boldsymbol{\psi}$ is given by :

$$\frac{1}{r^2 \sin\theta}\left[\sin\theta \frac{\partial}{\partial r}\left(r^2 \frac{\partial}{\partial r}\right) + \frac{\partial}{\partial \theta}\left(\sin\theta \frac{\partial}{\partial \theta}\right) + \frac{1}{\sin\theta}\left(\frac{\partial^2}{\partial \phi^2}\right)\right]\boldsymbol{\psi}(\boldsymbol{r}, \boldsymbol{\theta}, \boldsymbol{\phi}) = 0$$

$$\boldsymbol{\psi}(\boldsymbol{r}, \boldsymbol{\theta}, \boldsymbol{\phi}) = \sum_{l,m} \boldsymbol{\psi}_{\boldsymbol{l,m}}(\boldsymbol{r}, \boldsymbol{\theta}, \boldsymbol{\phi})$$

The wave function $\boldsymbol{\psi}(\boldsymbol{r}, \boldsymbol{\theta}, \boldsymbol{\phi})$, due to azimuthal symmetry has only r and θ dependence. Thus the solution of wave functions in terms of Legendre Polynomials can be given as :

$$\boldsymbol{\psi_{in}} = \sum_{l=0}^{\infty} A_l \; r^l \; P_l(\cos\theta) \qquad for \; r < a, \tag{4.6a}$$

$$\boldsymbol{\psi_{out}} = \sum_{l=0}^{\infty} (B_l \; r^l + C_l \, r^{-(l+1)}) P_l(\cos\theta) \qquad for \; r > a, \tag{4.6b}$$

Using the boundary conditions for continuation of tangential components of $\boldsymbol{E}$ fields, we get for $r = a$:

$$-\frac{1}{a}\frac{\partial \boldsymbol{\psi_{in}}}{\partial \theta}\Big|_{r=a} = -\frac{1}{a}\frac{\partial \boldsymbol{\psi_{out}}}{\partial \theta}\Big|_{r=a} \tag{4.7a}$$

and from normal components of displacement fields:

$$-\varepsilon_0 \varepsilon(\omega) \frac{\partial \boldsymbol{\psi_{in}}}{\partial r}\Big|_{r=a} = -\varepsilon_0 \varepsilon_d \frac{\partial \boldsymbol{\psi_{out}}}{\partial r}\Big|_{r=a} \tag{4.7b}$$

Now solving for the first order mode, i.e., $l = 1$ we get solutions [18]:

$$\boldsymbol{\psi_{in}} = -E_0 \; \frac{3\varepsilon_d}{\varepsilon(\omega) + 2\varepsilon_d} \quad r\cos\theta \qquad for \; r < a, \tag{4.8a}$$

$$\boldsymbol{\psi_{out}} = -E_0 \, r\cos\theta \; + E_0 \; \frac{\varepsilon - \varepsilon_d}{\varepsilon(\omega) + 2\varepsilon_d} a^3 \; \frac{\cos\theta}{r^2} \qquad for \; r > a, \tag{4.8b}$$

Defining the polarizing vector **P**, we represent $\boldsymbol{\psi_{out}}$ as :

(4.9)

$$\boldsymbol{\psi_{out}} = -E_0\, r\cos\theta \;+\; \frac{\boldsymbol{P}.\boldsymbol{r}}{4\pi\varepsilon_0\varepsilon_d r^3}$$

$$\boldsymbol{P} = \quad 4\pi\varepsilon_0\varepsilon_d \frac{\varepsilon-\varepsilon_d}{\varepsilon(\omega)+2\varepsilon_d} a^3\, \boldsymbol{E} \quad = \quad \varepsilon_0\varepsilon_d\, \alpha\, \boldsymbol{E} \tag{4.10}$$

where polarizability takes the frequency dependent form:

$$\alpha\,(\omega) = \quad 4\pi \frac{\varepsilon(\omega)-\varepsilon_d}{\varepsilon(\omega)+2\varepsilon_d} a^3 \tag{4.11}$$

It is to be noted that the Localized Surface Plasmons considered here are different from SPPs discussed in the previous chapter where SPPs are characterized by its dispersion relation:

$$k_x = \frac{\omega}{c}\sqrt{\frac{\varepsilon_d\varepsilon_m}{\varepsilon_d+\varepsilon_m}}$$

and represent a propagating surface wave. In contrast LSPs are confined to curved metal surfaces which are characterized by discrete and complex frequency dependent permittivity and the resonant condition which is defined by the shape and the geometry of the nanostructure. The LSPs in these particles can be excited by direct illumination by electromagnetic radiation of appropriate frequency irrespective of the wave vector. Hence the condition to match the wave vector to couple to plasmon modes is not required in this case.

LSPs can also be attributed to structures present on the metal surface or due to roughness of the surface. If the LSP resonant frequency lies close to surface plasmon frequency, LSPs can decay into surface plasmons while, in turn, the SPPs propagating on the surface can couple into LSPs. Thus it is important to realize the contribution of surface defects or roughness for the scattering of SPPs. Due to the small volume of the nanostructures, the field enhancement is observed due to presence of LSP resonances. This phenomenon of field enhancement leads to very interesting applications like Surface Enhanced Raman Scattering (SERS) and photovoltaic current enhancement and aperture-less Scanning near-field microscopy [25, 26].

4.4 Scattering of Surface Plasmons

The scattering of surface plasmon (SP) is characterized by three effects: scattering of SP to another direction as a result of reflection, scattering of SP modes to out-of-plane propagating light and propagation of SPs through or over the surface feature. Like other scattering phenomenon, the scattering of SPs depends upon the geometry/size (with comparison to the SPP wavelength) and dielectric constant of the surface feature.

The process of scattering phenomenon due to small particles, as mentioned in last section, has caught considerable interest, leading to enhancement in efficiency of fluorescence imaging, photovoltaics and quantum optics. We study here the effect of scattering which exhibits a scattering cross-section much larger than physical cross-section of the particle. As the continuation of previous section, we consider scattering due to a sphere (radius a << λ), which can be modeled as a point spherical dipole whose scattering cross-section (C_s) and absorption cross-section (C_a) can be defined as [27]:

$$C_s = \frac{1}{6\pi}\left(\frac{2\pi}{\lambda}\right)^4 |\alpha|^2 \quad and \quad C_a = \frac{2\pi}{\lambda} Im[\alpha]$$

where α is the polarizability as derived in the previous section.

$$\alpha\,(\omega) = \quad 4\pi \frac{\varepsilon(\omega)-\varepsilon_d}{\varepsilon(\omega)+2\varepsilon_d} a^3 \quad = \quad 3V \left[\frac{\varepsilon(\omega)-\varepsilon_d}{\varepsilon(\omega)+2\varepsilon_d}\right] \tag{4.12}$$

We note here that when $\varepsilon(\omega) = -2\varepsilon_d$, the particle polarizability attains bulk resonance frequency. We see that the scattering cross-section is very large near the bulk resonance frequency. The cross-sections defined above are valid only for small particles i.e. a << λ. As the particle size increases, dynamic depolarization, formation of multi-poles and radiation dampening effects cannot be neglected.

Substituting the values of frequency dependent dielectric constant, derived using Drude model (eq. (2.10)) i.e.

$$\varepsilon_m(\omega) = \left(1 - \frac{{\omega_p}^2}{\omega^2 + i\gamma\omega}\right) \tag{4.13}$$

we get

$$\alpha\,(\omega) \;\; = \;\; 3V\,\left(\frac{{\omega_p}^2}{\omega_p^2 - 3\omega^2 + i\gamma\omega}\right) \tag{4.14}$$

Thus, the bulk plasmon frequency for a spherical nanoparticle is related to plasma frequency

$$\omega = \sqrt{3}\,\omega_p = \omega_{bulk}.$$

4.5 Extraordinary transmission through Sub-Wavelength Apertures

One of the most exciting and intriguing phenomena related to plasmonics has been that of transmission properties of single apertures in a thin metal film and the enhanced transmission through periodic and aperiodic hole arrays. In this section, we begin the discussion with the transmission properties of sub-wavelength hole arrays and then discuss the role of surface plasmons in enhanced transmission.

The optical properties of a single aperture in a infinite perfect conductor has been defined by principle of Huygens-Fresnel diffraction. The scalar mathematical form for the problem, as defined by Kirchhoff, requires the fields at the aperture which are approximated equal to incident field at the hole. This assumption might be considered true when the aperture is much larger when compared to the wavelength, as diffracted field is relatively small on the screen, that would not violate the boundary conditions. The intensity distribution of the transmitted field in this case is essentially given in terms of first order Bessel functions and transmission pattern defined by Airy function. The transmission coefficient, T, defined by the intensity of transmitted field over incident intensity over the aperture area is close to 1 ($T \cong 1$.). However, it is noted that the Kirchhoff's approximation doesn't hold true when the aperture is much smaller than the wavelength. The transmission through sub-wavelength

aperture was first explained by Rayleigh and analytical expression was derived by Bethe, which is given by [31]:

$$T = \frac{64}{27\,\pi^2}\,(kr)^4 \tag{4.15}$$

Note that transmission through the hole is very weak and is of the order of $\left(\frac{r}{\lambda}\right)^4$. This relation is only defined for an infinitely thin film. For a practical case for thin film of finite conductivity and thickness, *h*, the transmission further decreases exponentially with *h*. We are interested in the fields tunneling through the hole, i.e., the hole diameter is small enough to allow any propagation modes inside the aperture (i.e. d < $\lambda/2$). The effect was contributed to the presence of localized surface plasmons (LSP) modes of the aperture. Degiron *et al.* [30] experimentally captured the presence of LSPs at the interface of the film using high energy electron beam induced surface plasmon emission (Fig.4.4).

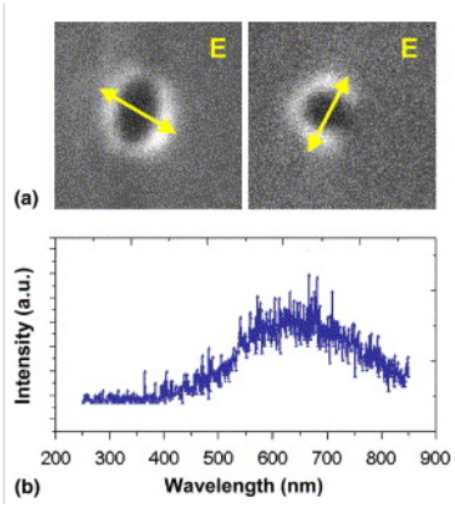

Fig. 4.4: (a) High electron micrograph images of two orthogonal polarizations of LSP located at the interface of the hole aperture. (b) Transmission spectrum obtained in the micrograph [30]

Similar effect was observed for rectangular and square apertures and direction dependent LSP modes were observed. The results also indicated that the LSP modes of each aperture in an array could also interact with one another, which can be controlled by appropriate arrangement of the apertures in the array in periodic and aperiodic fashion [30]. Ebbesen *et al.* [7] , observed an unusual transmission spectra from a square array of sub-wavelength holes and found peaks at wavelengths larger than diameter of the cylinder which exceeded the unity transmission coefficient by orders of magnitude. The existence of the peaks was attributed to surface plasmon modes which were excited using a grating coupler. It was shown that for a normally incident light over the square lattice the peaks are approximated by:

$$\lambda_{peak}(i.j) = P\frac{1}{\sqrt{i^2+j^2}}\, n_{spp} = P\frac{1}{\sqrt{i^2+j^2}}\sqrt{\frac{\varepsilon_m\varepsilon_d}{\varepsilon_m+\varepsilon_d}}$$

where P is the lattice constant and *i* and *j* are the scattering orders of the hole array. Thus the transmission pattern for a plane wave impinging on the hole array is defined by the interference and diffraction due to each aperture of the hole array. The corrugations on the input side determine the transmission peaks that diffracts in all directions when passing through the sub-wavelength aperture. The diffraction pattern of the bare hole can also be engineered by adding the periodic or aperiodic structure to the exit plan, where selective scattering and interference phenomenon defines the shape of the beam. Lezec *et al.* [5] demonstrated the phenomenon wherein a bull's-eye structure formed by periodic grooves around a sub-wavelength hole where the transmission through the hole can be engineered by the periodic groove on the surface. Similarly, the beam shaping device was demonstrated using the groove array on the output side of the Ag film.

The phenomenon of frequency selective enhanced transmission through sub-wavelength apertures has also been demonstrated using periodic and aperiodic aperture and groove arrays [28-30]. The phenomenon mediated by LSPs or aperture waveguide resonances has been

explored for some very intriguing applications like optical filtering, enhancement of fluorescent molecules, near-field imaging and optical and thermal switching using non-linear materials. Since the SPPs are highly sensitive to the refractive index of the surrounding dielectric medium, thus with an effective control over the refractive index one can control the optical transmission from the periodic structures and resonances in metallic structures. Using medium composed of ferroelectric or electro-optic, non-linear medium one can change the resonant conditions of light tunneling through the aperture and can design all optical devices.

4.6 Numerical Techniques

Surface plasmons, as discussed in the previous chapters, can be described by Maxwell's equations and the field solutions for SPPs can be effectively obtained using different numerical techniques. In this section we will discuss the common electromagnetic simulation methods as well as the equivalent methods used to solve these problems.

While modeling plasmonic structures certain factors specific to surface plasmons need to be addressed. Firstly, the dielectric constant of metals is to be defined in complex form, which is also inherently a function of frequency. Thus the numerical technique for solving fields in the presence of metals is required to be modeled using Drude-Lorenz model (eq. (2.11a, 2.11b)). It is also to be noted that even the Lorenz-Drude model does not account for interband transitions in metals, the simulation technique needs to be programmed using experimental data. Secondly, as the fields are highly confined to the metal-dielectric interface and decay exponentially away from the surface, a very fine mesh size is required, usually of the orders of $\frac{\lambda}{10}$ to $\frac{\lambda}{100}$ depending upon the application. The accuracy of the simulation results for nanoscale plasmonic devices depends highly on the mesh size and the geometry defined (as for curved or pointed surfaces, non-uniform mesh yields more accurate results). Different finite-difference techniques, where the differential equations are approximated by finite differences, are used model electromagnetic devices; we discuss here the basic concept of

these techniques (FDFD and FDTD) without going into much detail.

Finite Difference Frequency Domain (FDFD): As in finite difference methods, a continuous problem involving electromagnetic fields is converted to a discrete problem where the fields are calculated only at the points defined by the mesh. Later the fields are approximated over the entire region. In FDFD technique the fields are calculated at the grid of the nodes. The differential equation in special domain is approximated to accuracy of second order using the Taylor's series expansion, given by:

$$\left.\frac{df}{dx}\right|_{x_0} = \frac{f(x_0+\Delta x)-f(x_0-\Delta x)}{2\Delta x} + order\,[(\Delta x)^2] + \cdots \tag{4.16}$$

where Δx is defined by the mesh size. Similarly, the value of a function at a point, $\boldsymbol{p_{ijk}}$, in three dimensions defined by coordinates $(x_i\,, y_j\,, z_k)$ can be approximated. For a 1D problem with uniform grid, $x_i = i\Delta x$, the central-difference formula gives the relation:

$$\left.\frac{df\ (x_i)}{dx}\right|_i \cong \frac{f(i+1)-f(i-1)}{2\Delta x} \tag{4.17}$$

Similarly the second order differential takes the form :

$$\left.\frac{d^2f\ (x_i)}{dx^2}\right|_i \cong \frac{f(i+1)-2f(i)+f(i-1)}{(\Delta x)^2} \tag{4.18}$$

By using the above approximation, the second order wave equation obtained from Maxwell's equations can be deduced in terms of finite differences.

$$\nabla \times \nabla \times \boldsymbol{E}(\boldsymbol{r}) - k^2(r)\boldsymbol{E}(\boldsymbol{r}) = -i\omega\mu_0\,\boldsymbol{J}(\boldsymbol{r}) \tag{4.19}$$

Considering the two-dimensional case, for simplicity, where **E** field vector has no z-dependence, i.e., for a TE polarization, the above equation can be represented as:

$$\left[\frac{d^2}{dx^2}+\frac{d^2}{dy^2}\right]\boldsymbol{E_z}(\boldsymbol{r}) - k^2(r)\boldsymbol{E_z}(\boldsymbol{r}) = -i\omega\mu_0\,\boldsymbol{J_z}(\boldsymbol{r})$$

Considering a uniform rectangular mesh defined by $x_i = i\Delta x$ and $y_j = j\Delta y$, we get :

(4.20)

$$\frac{f(i+1,j)-2f(i,j)+f(i-1,j)}{(\Delta x)^2}+\frac{f(i,j+1)-2f(i,j)+f(i,j-1)}{(\Delta y)^2}+k^2(i,j)\,f(i,j)$$

$$= C\,\boldsymbol{J}(\boldsymbol{i},\boldsymbol{j}) \tag{4.23}$$

In the above equation $k^2(i,j)$ can be defined as ${k_0}^2\varepsilon_r(i,j,\omega)$ to account for dispersive properties of the metal. Thus the fields at a point can be calculated using fields at neighboring 2, 4 or 6 in case of one-, two-, or three- dimensional case. The equations can be later solved by solving the set of linear equation given by $\boldsymbol{A}\,\boldsymbol{x}=\boldsymbol{B}$**,** where B is defined by the source currents **J.** As can be seen from above argument, the FDFD technique yields a sparse matrix that can be solved efficiently.

Finite Difference Time Domain (FDTD): FDTD is a time domain technique that uses the similar concept of finite differences but in this case for time differential equations [33]. Thus the source free solutions for Faraday's law and Ampere's law can be given by:

$$\nabla X\,\boldsymbol{E}(\boldsymbol{t})=-\mu\,\frac{\partial \boldsymbol{H}(t)}{\partial t}\;\rightarrow\;\nabla X\,\boldsymbol{E}(\boldsymbol{t})\cong-\mu\,\frac{\boldsymbol{H}(t+\Delta t)-\boldsymbol{H}(t)}{\Delta t} \tag{4.21a}$$

$$\nabla X\,\boldsymbol{H}(\boldsymbol{t})=-\mu\,\frac{\partial \boldsymbol{E}(t)}{\partial t}\;\rightarrow\;\nabla X\,\boldsymbol{H}(\boldsymbol{t})\cong\varepsilon\,\frac{\boldsymbol{E}(t+\Delta t)-\boldsymbol{E}(t)}{\Delta t} \tag{4.21b}$$

The equations can also be represented as :

$$\nabla X\,\boldsymbol{E}(\boldsymbol{t})=-\mu\,\frac{\partial \boldsymbol{H}(t)}{\partial t}\;\rightarrow\;\nabla X\,\boldsymbol{E}(\boldsymbol{t})\cong-\mu\,\frac{\boldsymbol{H}(t+\Delta t/2)-\boldsymbol{H}(t-\Delta t/2)}{\Delta t} \tag{4.22a}$$

$$\nabla X\,\boldsymbol{H}(\boldsymbol{t})=-\mu\,\frac{\partial \boldsymbol{E}(t)}{\partial t}\;\rightarrow\;\nabla X\,\boldsymbol{H}(\boldsymbol{t}+\Delta t/2)\cong\varepsilon\,\frac{\boldsymbol{E}(t+\Delta t)-\boldsymbol{E}(t)}{\Delta t} \tag{4.22b}$$

We can see from the above equations that the right hand that we need to know **H** fields at time $(t+\Delta t)$ in order to compute **E** fields at time instant t. Thus the problem can be extremely difficult to solve. This can be solved by staggering **E** and **H** fields in time, where **H**

fields are computed at every $(\Delta t/2, t + \Delta t/2, 2t + \Delta t/2, \ldots)$ and **E** fields at $(0, \Delta t, t + \Delta t, \ldots)$. The eq. (4.22b) can be written as:

$$\boldsymbol{E}|_{(t+\Delta t)} = \boldsymbol{E}|_{(t)} + \frac{\varepsilon}{\Delta t} . \nabla X \boldsymbol{H}|_{(t+\Delta t/2)}$$

Thus the coefficients $\frac{\varepsilon}{\Delta t}$ can be computed beforehand and EM solutions using FDTD method can be computed. Next problem is to define fields in space in the grid (unit cell).

Yee in his 1966 paper described the technique to solve the Maxwell's curl equations on the grid points that are staggered in time as well as space. Thus the fields that are continuous in space are computed at discrete points staggered at points defined by the Yee cell [34]. A typical Yee cell in 1D, 2D and 3D is shown in Fig.4.6:

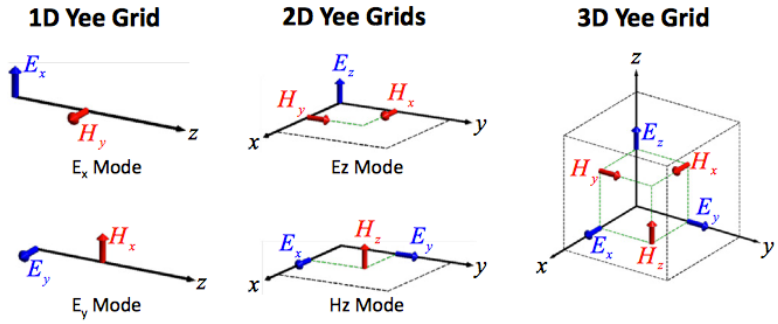

Fig. 4.5: Schematic showing Yee grid cell in 1D, 2D and 3D.

Thus the curl equations are given by:

$$\frac{\partial E_y}{\partial x} - \frac{\partial E_x}{\partial y} = -\mu \frac{\partial H_z}{\partial t} \rightarrow \frac{E_y^{i+1,j,k}\big|_t - E_y^{i,j,k}\big|_t}{\Delta x} - \frac{E_x^{i,j+1,k}\big|_t - E_x^{i,j,k}\big|_t}{\Delta y}$$

$$= -\mu \frac{\boldsymbol{H_z^{i,j,k}}\big|_{t+\frac{\Delta t}{2}} - \boldsymbol{H_z^{i,j,k}}\big|_{t-\frac{\Delta t}{2}}}{\Delta t}$$

$$\frac{\partial E_z}{\partial y} - \frac{\partial E_y}{\partial z} = -\mu \frac{\partial H_x}{\partial t} \rightarrow \frac{E_z^{i,j+1,k}\big|_t - E_z^{i,j,k}\big|_t}{\Delta y} - \frac{E_y^{i,j,k+1}\big|_t - E_y^{i,j,k}\big|_t}{\Delta z}$$

$$= -\mu \frac{\boldsymbol{H_x^{i,j,k}}\big|_{t+\frac{\Delta t}{2}} - \boldsymbol{H_x^{i,j,k}}\big|_{t-\frac{\Delta t}{2}}}{\Delta t}$$

$$\frac{\partial E_x}{\partial z} - \frac{\partial E_z}{\partial x} = -\mu \frac{\partial H_y}{\partial t} \rightarrow \frac{E_x^{i,j,k+1}\big|_t - E_x^{i,j,k}\big|_t}{\Delta z} - \frac{E_z^{i+1,j,k}\big|_t - E_z^{i,j,k}\big|_t}{\Delta x}$$

$$= -\mu \frac{\boldsymbol{H_y^{i,j,k}}\big|_{\boldsymbol{t+\frac{\Delta t}{2}}} - \boldsymbol{H_y^{i,j,k}}\big|_{\boldsymbol{t-\frac{\Delta t}{2}}}}{\Delta t}$$

and

$$\frac{\partial H_y}{\partial x} - \frac{\partial H_x}{\partial y} = -\varepsilon \frac{\partial E_z}{\partial t} \rightarrow \frac{H_y^{i+1,j,k}\big|_{\boldsymbol{t+\frac{\Delta t}{2}}} - H_y^{i,j,k}\big|_{\boldsymbol{t+\frac{\Delta t}{2}}}}{\Delta x} - \frac{H_x^{i,j+1,k}\big|_{\boldsymbol{t+\frac{\Delta t}{2}}} - H_x^{i,j,k}\big|_{\boldsymbol{t+\frac{\Delta t}{2}}}}{\Delta y}$$

$$= -\varepsilon \frac{\boldsymbol{E_z^{i,j,k}}\big|_{\boldsymbol{t+\Delta t}} - \boldsymbol{E_z^{i,j,k}}\big|_{\boldsymbol{t}}}{\Delta t}$$

$$\frac{\partial H_z}{\partial y} - \frac{\partial H_y}{\partial z} = -\varepsilon \frac{\partial E_x}{\partial t} \rightarrow \frac{H_z^{i,j+1,k}\big|_{t+\frac{\Delta t}{2}} - H_z^{i,j,k}\big|_{t+\frac{\Delta t}{2}}}{\Delta y} - \frac{H_y^{i,j,k+1}\big|_{t+\frac{\Delta t}{2}} - H_y^{i,j,k}\big|_{t+\frac{\Delta t}{2}}}{\Delta z} = -\varepsilon \frac{\boldsymbol{E_x^{i,j,k}}\big|_{t+\Delta t} - \boldsymbol{E_x^{i,j,k}}\big|_{t}}{\Delta t}$$

$$\frac{\partial H_x}{\partial z} - \frac{\partial H_z}{\partial x} = -\varepsilon \frac{\partial E_y}{\partial t} \rightarrow \frac{H_x^{i,j,k+1}\big|_{\boldsymbol{t+\frac{\Delta t}{2}}} - H_x^{i,j,k}\big|_{\boldsymbol{t+\frac{\Delta t}{2}}}}{\Delta z} - \frac{H_z^{i+1,j,k}\big|_{\boldsymbol{t+\frac{\Delta t}{2}}} - H_z^{i,j,k}\big|_{\boldsymbol{t+\frac{\Delta t}{2}}}}{\Delta x}$$

$$= -\varepsilon \frac{\boldsymbol{E_x^{i,j,k}}\big|_{\boldsymbol{t+\Delta t}} - \boldsymbol{E_x^{i,j,k}}\big|_{\boldsymbol{t}}}{\Delta t} \tag{4.24}$$

We observe that in the Yee cell, the derivatives are central and are thus second order accurate. While modeling metals at optical frequencies using FDTD methods, the dispersive effects of permittivity is applied using auxiliary differential equation (ADE) [33]. These equations relate electric field **E** to the displacement fields **D.**

$$\boldsymbol{D} = \varepsilon(\omega)\boldsymbol{E}$$

where $\varepsilon(\omega)$ is given by the Lorenz-Drude model as $\varepsilon(\omega) = \frac{{\omega_0}^2}{({\omega_0}^2 - \omega^2) - i\gamma\omega}$. Thus the inverse Fourier transform of the dispersion relation we get

$${\omega_0}^2 \boldsymbol{D} + \gamma \frac{\partial \boldsymbol{D}}{\partial t} + \frac{\partial^2 \boldsymbol{D}}{\partial t^2} = \omega^2 \varepsilon_0 \boldsymbol{E} \tag{4.25}$$

Using the ADE method **H** is obtained from **D** using the Ampere's law. The performance of FDTD method is almost similar to FDFD method but here the dispersive properties of metals have to be approximated using ADE method [34].

5. Guided-Wave Devices Based on Networked Plasmonic Waveguides

Photonic and optoelectronic technologies provide inherent advantage of faster processing speeds at low power levels when compared to electronic counterparts. One of the major hurdles in wide acceptance of these technologies has been the large feature size associated with them, limited by diffraction. Thus, photonic devices with sub-wavelength footprint are highly desired. One of the most promising approaches towards the miniaturization is achieved by harnessing surface plasmon polaritons within waveguide geometries. The field of plasmonics has facilitated research in all-optical nano-circuits, compact and integrable optical sources, modulators etc. [35-37]. Guided-wave structures to channel these SPPs with sub-wavelength confinement would form the backbone of such integrated optical technologies. In this chapter we will discuss the design rules and constraints in designing plasmon waveguide structures. Using interference effects within the waveguides we demonstrate different nanophotonic devices such as directional color-routers, filters and optical switch based on plasmon waveguide networks.

5.1 Sub-wavelength Confinement and Waveguide Configuration.

The minimum confinement, as mentioned previously, in case of dielectric waveguide is limited to $(\lambda/2\mathbf{n})$, defined by the waveguide mode size. In the case of plasmonic waveguide the confinement of the fields are set by the spatial extent of the evanescent fields which decay away from the interface. Different plasmon waveguide structures proposed include nanowire waveguide, metal-trench waveguide, MIM (metal-insulator-metal or MDM) and IMI (insulator-metal-insulator or DMD) planar waveguides, slot waveguide, coaxial waveguide, nanoparticle array based waveguide etc. [38-42]. We limit our discussion to three layer core based MIM and IMI waveguide geometries.

The dispersion relation, for a wave propagating in x-direction and considering infinite

geometry in y direction:

$$k_{mz}{}^2 + k_x{}^2 = \frac{\omega^2}{c^2}\,\varepsilon_m \tag{5.1}$$

$$k_{dz}{}^2 + k_x{}^2 = \frac{\omega^2}{c^2}\,\varepsilon_d\,, \tag{5.2}$$

For a guided mode to exist,

$$k_x{}^2 \geq \frac{\omega^2}{c^2}\,\varepsilon_d \tag{5.3}$$

Thus the spatial extent into the two media is given by:

$$k_{mz} = i\sqrt{\left(k_x{}^2 - \frac{\omega^2}{c^2}\,\varepsilon_m\right)} \tag{5.4a}$$

$$k_{dz} = i\sqrt{\left(k_x{}^2 - \frac{\omega^2}{c^2}\,\varepsilon_d\right)} \tag{5.4b}$$

From the above equation the spatial confinement in the dielectric is limited by the diffraction ($\lambda\,/2\mathbf{n}$), thus we obtain :

$$|k_{dz}| \leq \frac{2\pi}{\lambda}\,n_{diel} = \frac{\omega}{c}\,\sqrt{\varepsilon_d} \tag{5.5}$$

We can clearly see that the fields are more confined inside the metal as the rate of exponential decay is much faster:

$$|k_{mz}| \leq \frac{\omega}{c}\,\sqrt{\varepsilon_d} \tag{5.6}$$

Thus MIM waveguide structures showcases improved confinement at the cost of allowing increased field intensities inside the metal. The confinement factor Γ, is defined as ratio of power in the core region to the total power in the waveguide [43] :

$$\Gamma = \frac{Field\ intensity\ in\ core}{Total\ Field\ in\ the\ waveguide} = \frac{\int_{core} E_x H_y\ dz}{\int_{-\infty}^{\infty} E_x H_y\ dz} \tag{5.7}$$

The tradeoff between the propagation length and the field confinement as calculated by Zia *et al.* is plotted in Fig. 5.1.

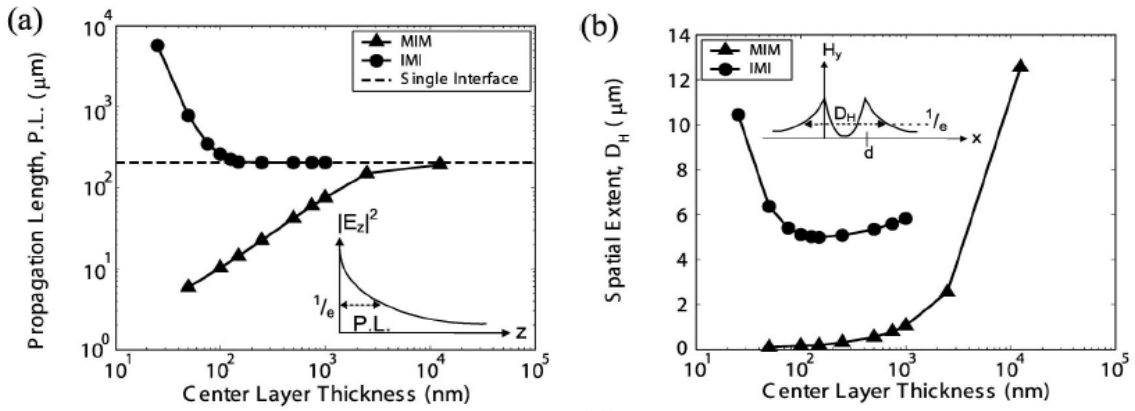

Fig. 5.1: Plots showing (a) propagation length and (b) spatial extent vs. center layer thickness for IMI and MIM waveguide based on Au-air at 1550 nm wavelength [43].

To achieve reasonable confinement the IMI waveguide requires very symmetric dielectric cladding, whereas for MIM waveguides, the spatial extent is restricted by the Ohmic losses in the metal as the fields penetrate only up to about skin depth into the metal. Since the MIM geometry allows us to place waveguides very close to each other, to design structure with very accurate mode dimensions, the MIM geometry is preferred for circuit-based designs. The modes in MIM plasmon waveguide structures can be excited using simple end-fire technique, where focused light beams when incident on the open end of the waveguide, excites the dominant mode of the waveguide.

5.2 Plasmon Waveguide Structures

In this section we discuss the behavior of different basic plasmon waveguide structures that are composed of planar metal-insulator-metal geometries, composed of silver and silicon dioxide (Ag-SiO_2-Ag waveguide). The results were obtained using a commercial EM solver, Lumerical FDTD solutions. The simulations were run for different optical frequencies. We will also present the different models that have been proposed (when applicable) for the structures.

The importance of understanding these waveguide components is necessary to describe the behavior and thus, reduce the reflections and hence cross-talk between different components. For our purpose we simulate the waveguide structures in 2D, and excite the waveguide at optical frequencies, 650nm and 750 nm. As we have seen in last chapter the plasmons are highly lossy in visible range as we go towards ultraviolet, thus we limit ourselves to design devices to longer visible wavelengths. However the propagation lengths are much longer at near-IR and optical communication wavelength, i.e., 1550 nm (restricted to 1550 due to high absorption in silicon at smaller wavelength), but due to adequate technologies in silicon photonics and optical fibers, available in the frequency regime we intend to design devices with smaller footprint at the higher frequencies.

L-bend Waveguide

The structure is composed of a sharp 90° bend in an MIM waveguide we simulate the structure with a 750 nm monochromatic plane wave source, that excites surface plasmon modes in the waveguide. We measure the transmission and reflection as a function of output waveguide width.

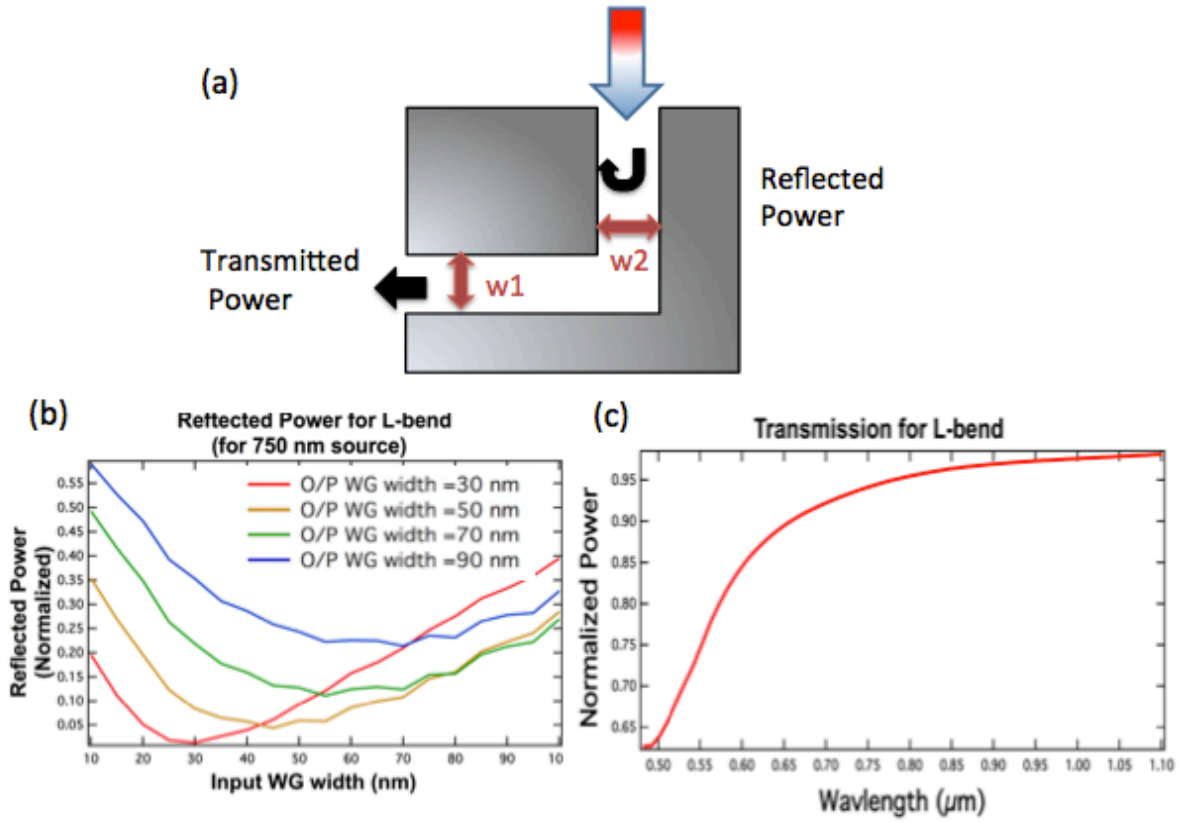

Fig. 5.2: L-bend Waveguide: (a) 2D Schematic of L bend MIM waveguide, (b) Simulation results for L bend waveguides. Plots show normalized reflected power with varying Input WG width, for different values of output WG, (c) plot shows the transmitted power for w1=w2= 50 nm.

We observe that plasmon waveguides suffer substantial reflection when bent sharply at 90° and thus introduces extra loss into the waveguides. The reflection suppressed by rounding the sharp edge around the bend slightly, or by introducing additional structure at the site of the bend to reduce the effective waveguide dimension. We observe that for small waveguide dimensions, the L-bend follows the transmission line model where the reflection coefficient, R, is given by:

$$R = \left|\frac{Z_L - Z_{in}}{Z_L + Z_{in}}\right|^2 = \left|\frac{Z_{MIM}(w_{in}) - Z_{MIM}(w_{out})}{Z_{MIM}(w_{in}) + Z_{MIM}(w_{out})}\right|^2 \quad (5.8)$$

where w_{in} and w_{out} represent the width of input and output waveguide respectively. The impedance of MIM plasmon waveguide is given by:

$$Z_{MIM} = \frac{\beta_{TEM}}{\omega \varepsilon_0} w \tag{5.9}$$

This approximation is valid for TE modes (as well as Quasi-TEM modes). Note when the $Z_L = Z_{in}$, i.e., the input waveguide width equals output waveguide width, the reflection should go to zero. This is valid in our case as long as $\lambda_{SPP} > w$ (waveguide width), under this limit, the plasmon modes are coupled to one another and hence no standing wave can exist in the waveguide. The behavior deviates from the model when waveguide width comparable to the wavelength of SPP. This reflection is also reduced for higher wavelength for same waveguide dimensions [40]. The reflection in the L-bend increases as the width of the waveguide (input and output) increases due to increase in effective width at the bend; this can be overcome by using a curved bend or tapered bend keeping the waveguide width constant throughout.

T-bend Waveguide

T bend in MIM plasmon waveguide, like a conventional waveguide, act as a power splitting element and divides the power equally among the two waveguides provided the width of the two waveguides is equal. We see from the plots in Fig. 5.3 that the T-bend waveguide complies with the transmission line model more accurately. Here the condition of zero reflection is met when the input waveguide width is double than that of the output waveguide.

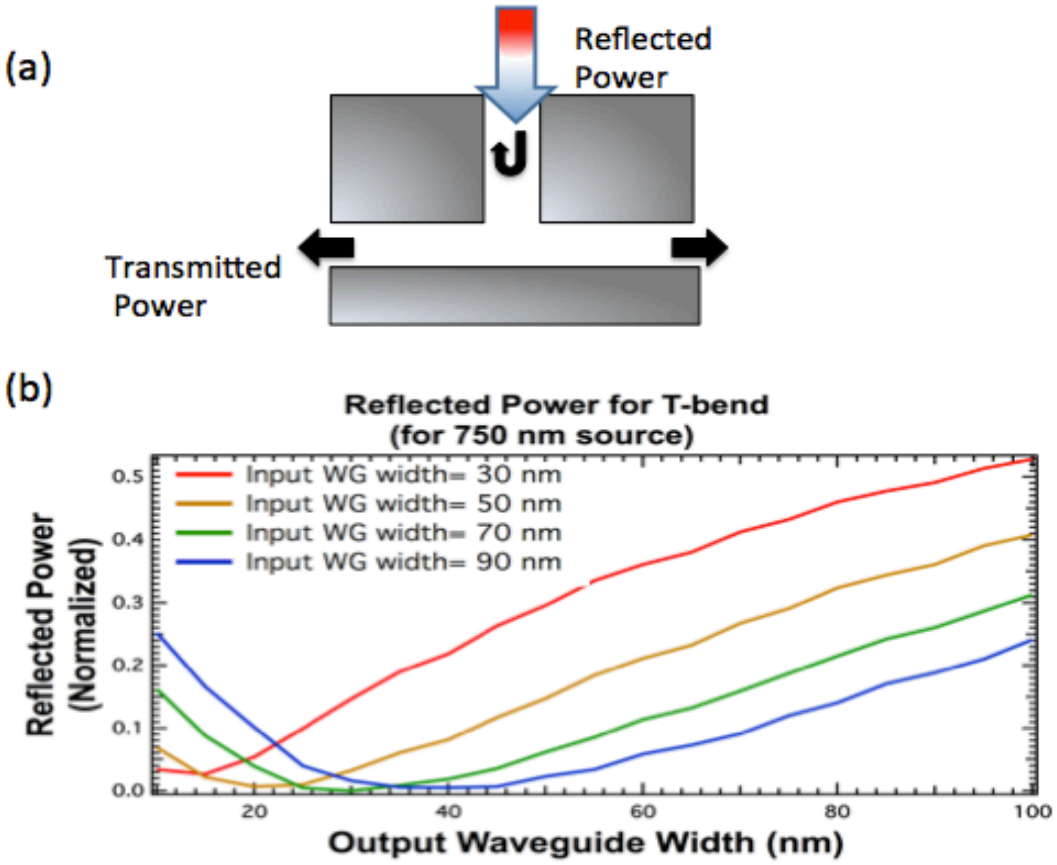

Fig. 5.3: T-bend Waveguide: (a) 2D Schematic of T bend MIM waveguide, (b) Simulation results for T bend waveguides. Plots show normalized reflected power vs. output waveguide width.

The transmission line model in this case is modified to:

$$R = \left|\frac{Z_L - Z_{in}}{Z_L + Z_{in}}\right|^2 = \left|\frac{2Z_{MIM}(w_{in}) - Z_{MIM}(w_{out})}{2Z_{MIM}(w_{in}) + Z_{MIM}(w_{out})}\right|^2 \quad (5.10)$$

We see from the plots above that the T-bend structure abides by the model relatively well.

Side-Waveguide Divider

Here we demonstrate the simulation results of a similar geometry as the T-bend, but side waveguide branches out of the main waveguide. Such structure could be crucial while designing plasmon based nano-circuits.

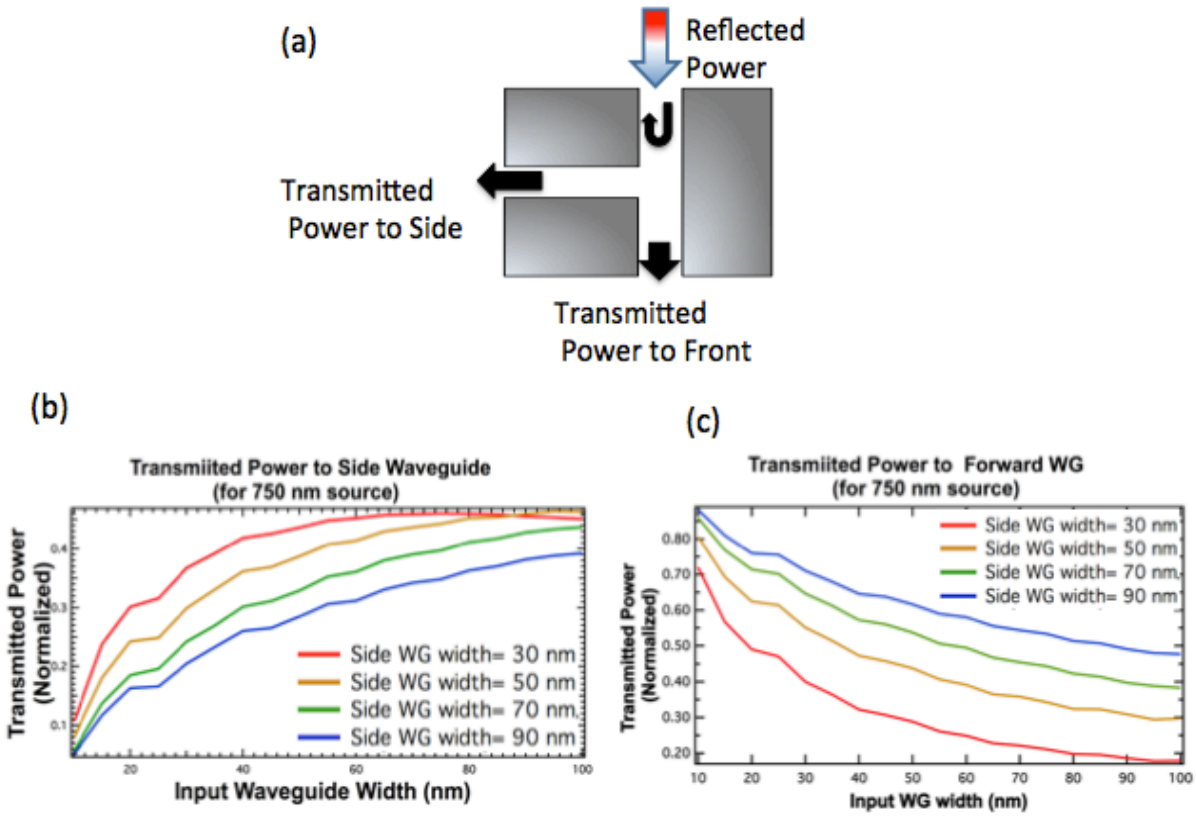

Fig. 5.4: Side-port Waveguide: (a) 2D Schematic of Side port in MIM waveguide, (b) Simulation results for Side-port waveguide structure. Plot shows normalized transmitted power to side WG and (c) shows normalized transmitted power to Forward WG vs. output waveguide width

We observed that the transmission to the side port is large when the side waveguide is narrower, while when the side port width is increased, the transmission to the side port is decreased. Almost 50:50 split in power is observed when the side waveguide and main transmission waveguide widths are equal. It is also observed that the transmission is more in the waveguide with smaller side waveguide width, providing a low impedance path. Also when the width of the side waveguide is increased, the gap or discontinuity in the input waveguide increases leading larger reflected power. The reflection in the input waveguide increases as the width of the input waveguide is decreased showcasing SPP with longer λ_{SP}.

4-port Splitter

One of the interesting and comparatively widely studied waveguide components is a 4-port splitter (4-way network, X-junction).

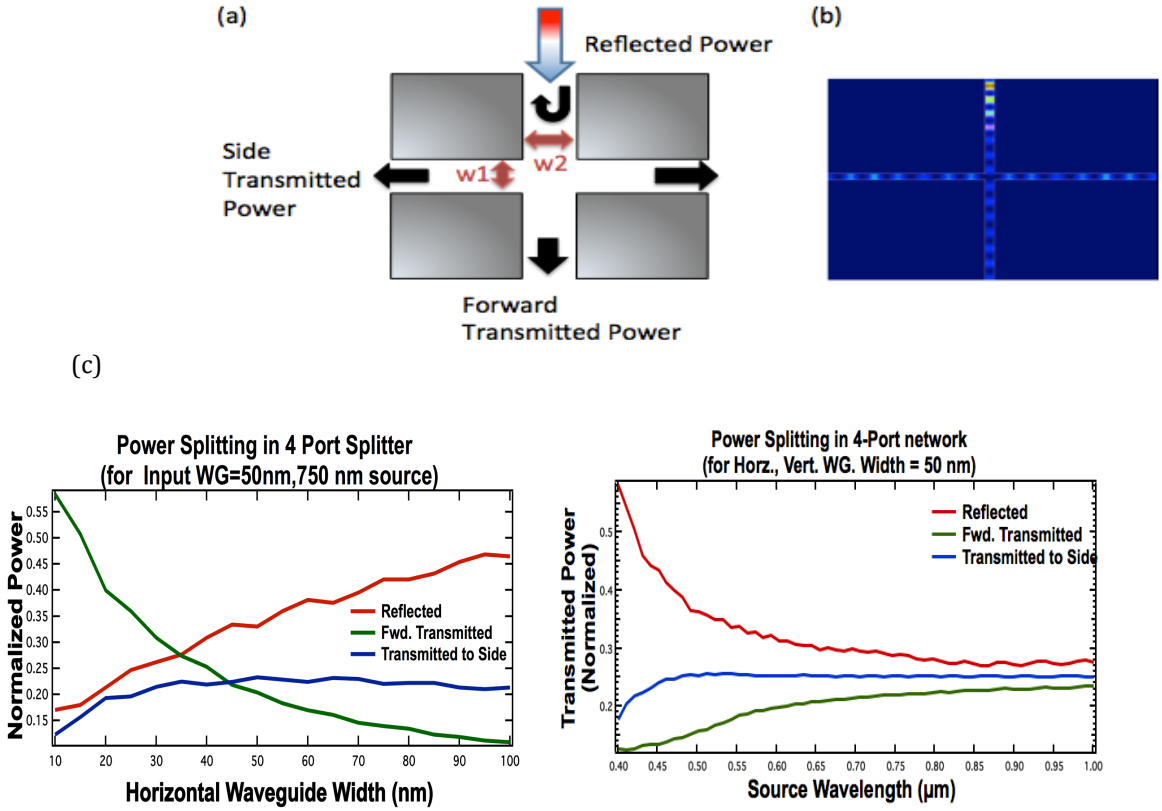

Fig. 5.5: 4 Port Splitter: 2D color plots for 4 port-network. To avoid reflection from the side ports, side waveguides are modeled as infinitely long, using PML boundary condition. (a), (b) Schematic and simulation screen-shot for 4-port network. Only one waveguide is excited with 750 nm source and the transmission is measured at the four ports. (c) shows the measured output power at the four ports vs. horizontal waveguide width for w2 = 50 nm (left) and transmission through different ports of 4-port splitter

for w1=w2=50 nm (right). The device behaves as an equal power splitting element at longer wavelengths.

We can clearly see from Fig. 5.5 that the 4-port network acts a 4 way equal power splitter element when the two waveguides are of equal width. The 4-port network can also be used as a unit cell for dividing complex waveguide network structures and can be designed for uneven transmission by varying the ratio of horizontal and vertical waveguide widths. It can also be noticed that when the width of horizontal waveguide is large as compared to the vertical waveguide, the SPPs propagating in the vertical waveguide see high impedance node (open circuit) and most of the wave is reflected back. On the contrary if the width of horizontal waveguide is small as compared to the vertical waveguide, the SPPs propagating in the vertical waveguide jump over the node and are transmitted in the forward direction, while only negligible power is transferred to the side waveguides. Similarly, other devices, stubs, Fabry-Perot cavities (open-ended plasmon waveguide resonator) structures have been demonstrated [44].

5.3 Networked Plasmonic Waveguides (NPW) and Devices

Based on the results obtained in the previous section and the last chapter, we can find the appropriate width of the waveguides and the propagation length as well as the frequency of operation. We now utilize the phenomenon of interference between two SPPs and design devices like color router and directional filter and optical switch based on plasmon waveguide network.

2 × 1 Networked Plasmonic Waveguides

In this geometry we cascade two 4-Port networks horizontally such that the horizontal waveguide of the two 4-Port networks form a interference network which also acts as a

resonant cavity. Here the two input waveguides are simultaneously excited. Using the concept of 4-port network, we know power splits at the 4-port junction and some power is transmitted to the common horizontal-waveguide. Now the length D, of the common side-waveguide can be varied to cause destructive and constructive interference at the waveguide junction. Thus by varying the length D now the splitting at the two original 4-port waveguide junctions can be modified. Through the simulations we see that at certain dimension D, the SPPs travelling in the vertical waveguide get canceled due to destructive interference with the SPPs introduced in the vertical waveguide by horizontal waveguide at the power splitting element. Thus we observe different transmission bands in the plots of Fig. 5.6. Using this property of the waveguide network, when we change the angle of the source illumination, the path length difference is introduced in the two vertical waveguides and hence the interference between the two SPPs at the common waveguide is also modified. As can be seen for the plots, different transmission outputs can be obtained at different angles.

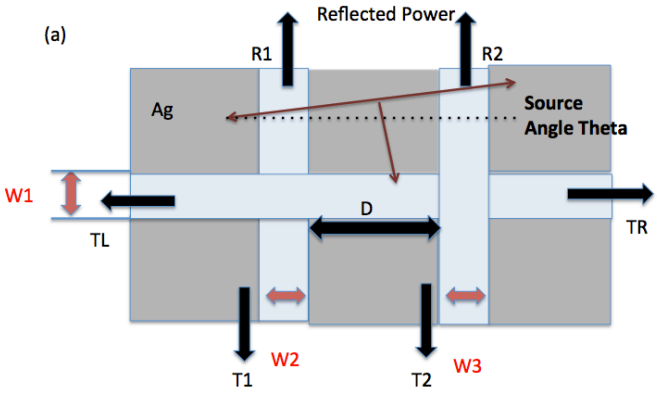

(b)

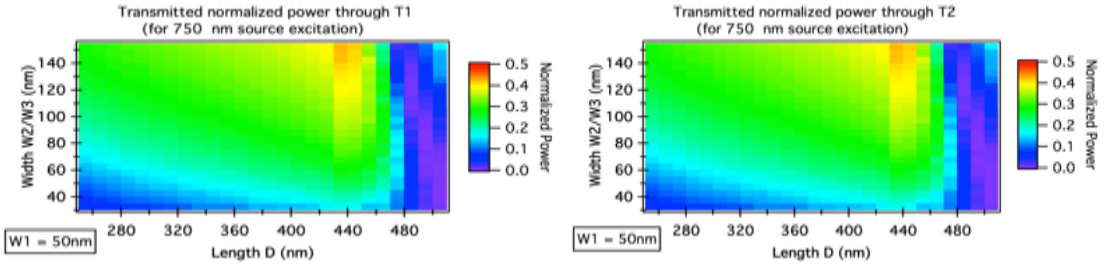

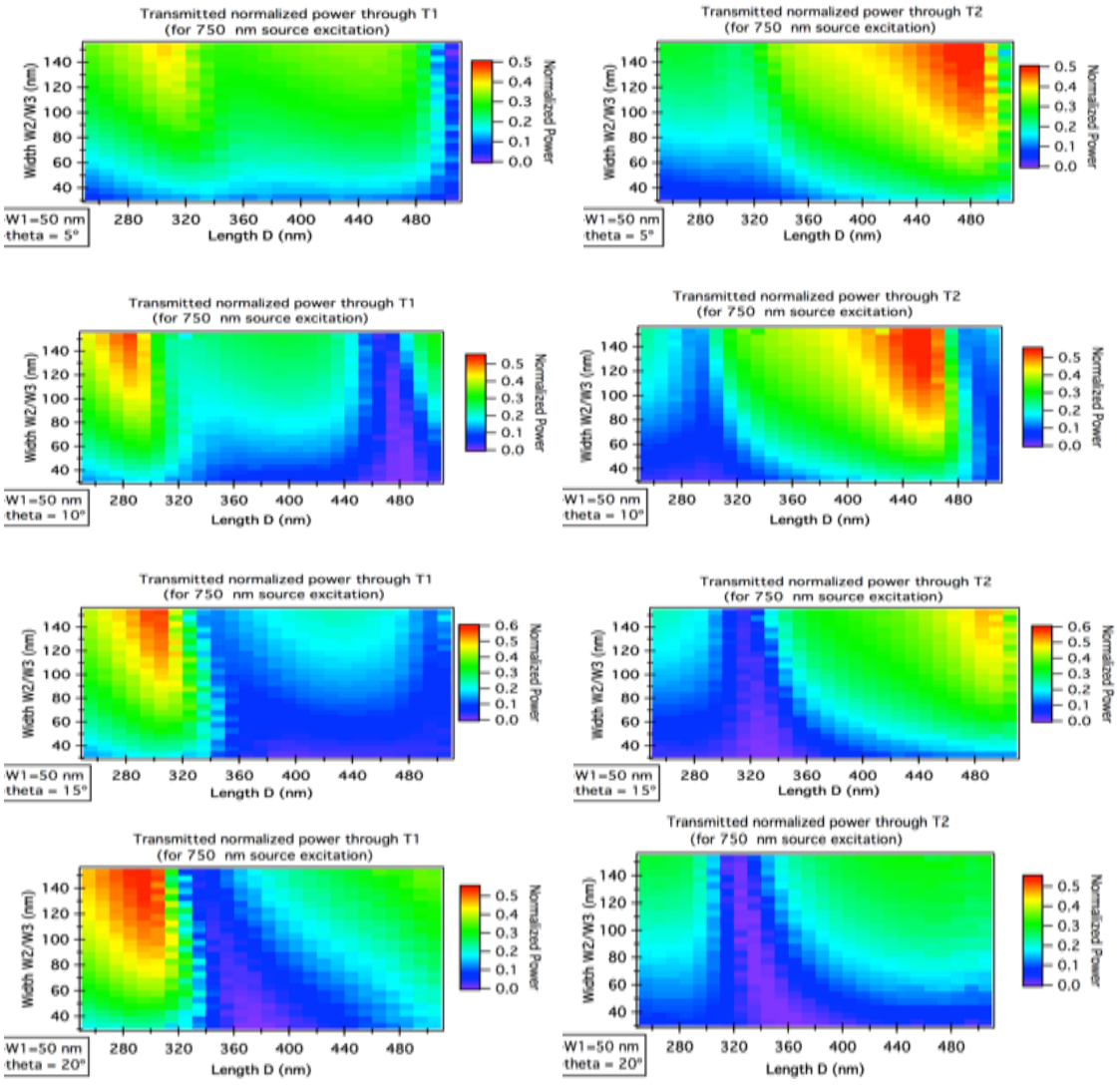

Fig. 5.6: (a) Schematic of 2 × 1 Networked Plasmonic Waveguides. The angle of the input source is varied from 0° *to* 20°, all the ports are perfectly matched through PML boundary condition. (b) 2D image plot for transmission through the two output ports. The plots show the transmission for different vertical waveguide width (y-axis) where W2 is kept equal to W3, while the x-axis shows the transmission for different values of D, length of the common horizontal waveguide. The plots are given for different angles of incidence $(0°, 5°, 10°, 15°, 20°)$ while the value of W1 (width of horizontal waveguide) is kept constant.

Note that the wavelength of SPPs depend on the width of the waveguide, thus the modification in transmission due to interference in the common waveguide will happen at

different values of length D. Similar argument is also valid if we change the wavelength of the excitation source. The plots shown above are for 750 nm source wavelength. Using the data from above, different directional devices can be designed.

2 X 2 Waveguide Network

We further modify the design where intersection of 2 vertical and 2 horizontal waveguide form a 2 × 2 Networked Plasmonic Waveguides (NPW). The geometry of 2 × 2 NPW is shown in Fig.5.7:

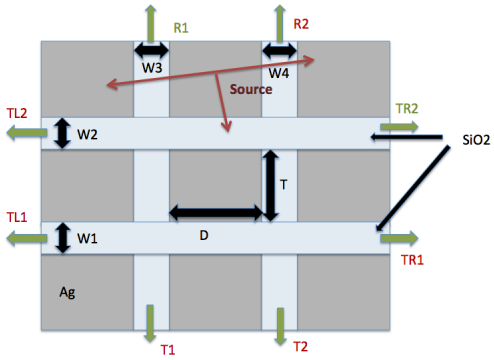

Fig. 5.7: Schematic of 2 × 2 Networked Plasmonic Waveguides

The 2 × 2 NPW utilizes the effect of the interference between SPPs in effectively 4 waveguides, i.e., two internal horizontal as well as the vertical waveguides. Thus now the parameters D and T can be varied to design and improve performance of different directional devices. We now demonstrate different devices designed using 2 × 2 NPW.

Directional Filter

As observed from 2 × 1 NPW (Fig. 5.5(a)), the output at the two output ports T1 and T2 can be modulated by introducing a phase difference between the two input ports, we propose directional filter device based upon 2 × 2 NPW as demonstrated in Fig. (5.8):

(a)

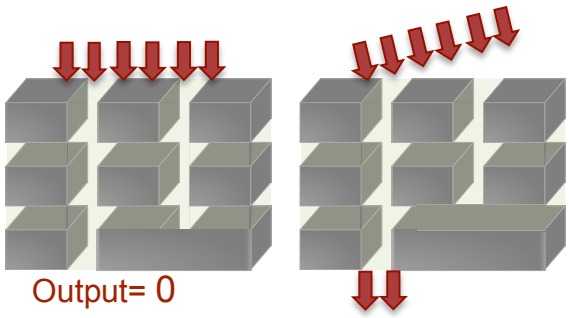

(b)

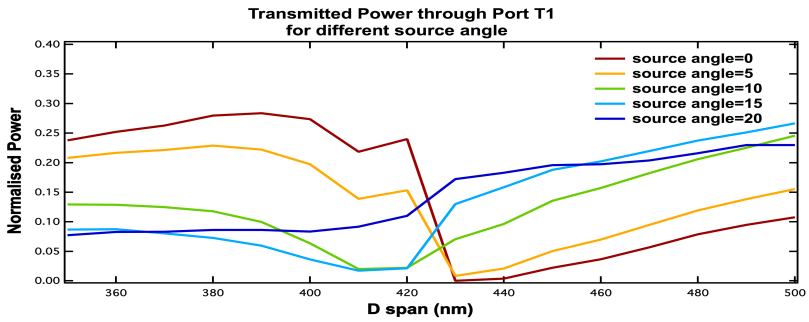

(c)

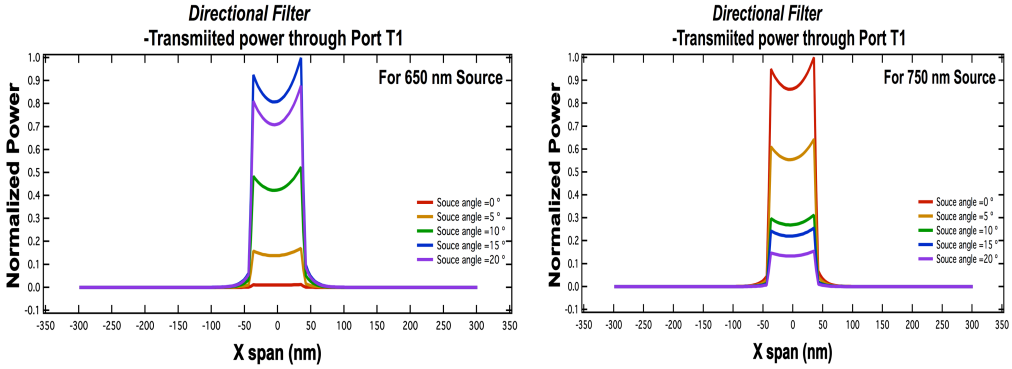

Fig. 5.8: NPW based directional filter (a) Schematic showing operation of directional filter based on 2x2 waveguide network, (b) plot showing power transmitted through port T1 with different length D. (c) shows the directional filter for different angles for 650 nm (left) and 750 nm (right) source excitation, respectively.

As can been seen from Fig. 5.8(b), different transmission levels can be obtained for different angle for a particular D. For example, at length D = 400nm, the transmission can be varied from max at 0º to minimum at 20º. Note that the output at port 2 is different than port 1 thus the device can be used as a single or two port device based on the device geometry and how

the outputs are being measured. The plots in Fig. 5.8(c) show varied transmission output for a single output port device for 650 nm and 750 nm source excitation.

Directional Optical Switch

Based on similar concept, the variable lengths and waveguide width can be modified to design an optical switch. The diagram in Fig. 5.9(a) shows a 2-bit optical switch where the outputs at port T1 and T2 can be modulated by changing the direction of the light, or by inducing phase change between the two input ports.

(a)

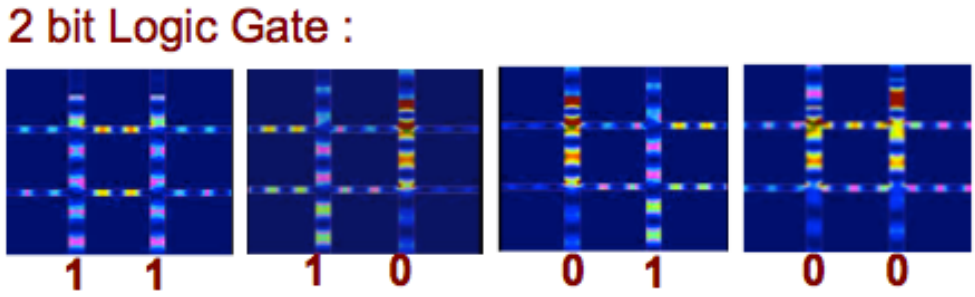

(b)

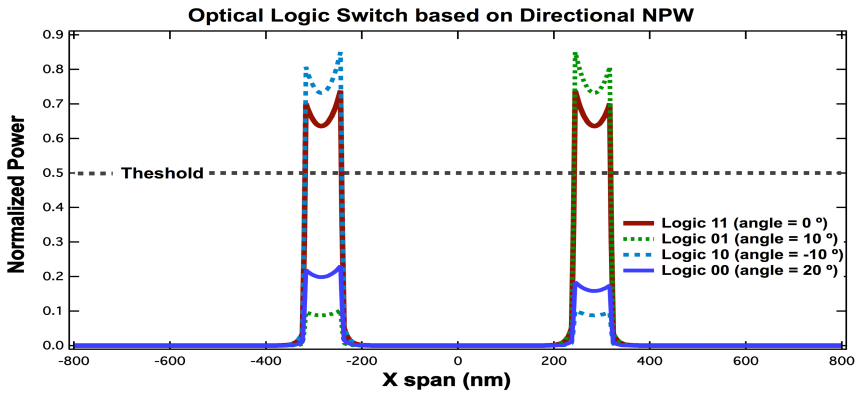

Fig. 5.9: 2-bit optical Switch (a) Steady state Simulation screen shots 750 nm source showing the field intensities at the two output waveguides. (b) plots represent an operation of NPW as optical switch.

For operation of the device as an optical switch, an optimal threshold level can be set, thus enabling the device to provide all 4 output combinations for the 2-bit switch. As seen from the above figure (Fig. 5.9 (a)), the output at the other side ports can be extracted to generate a 6-bit switch (or 8-bit by including the reflection ports).

Directional Color router

We also demonstrate an optical color router based on 2 × 2 plasmonic waveguide networks (Fig. 5.10 (a)) where the device can be used as an color router as well as an color mixer. The simulation results have been obtained for 750 nm and 650 nm wavelength sources. Due to the symmetry of the device, the color routing to the ports can be switched by changing the input source excitation by 180º.

(a)

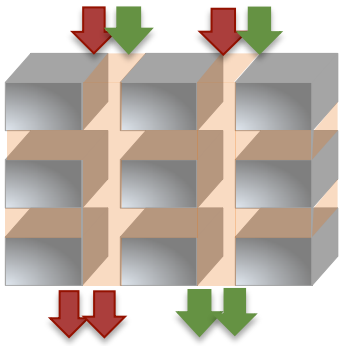

(b)

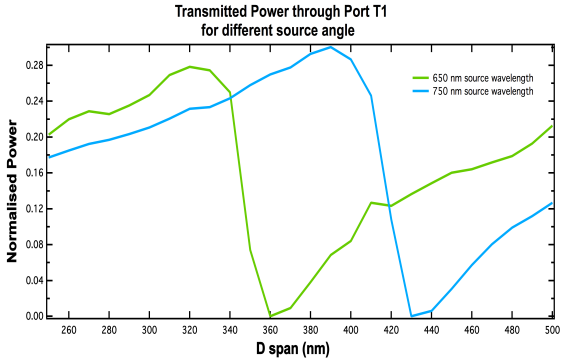

(c)

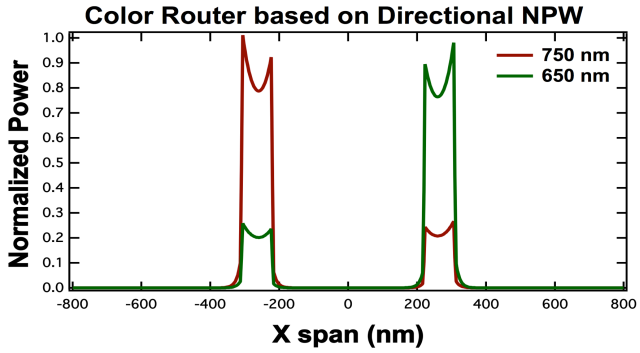

Fig. 5.10: Schematic showing directional color router using 2 X 2 NPW.

The plots in Fig. 5.10 (b) show, for different values of length D, varied values of transmission for the two wavelengths can be achieved. At D = 410 nm, the 650 nm source excitation can be guided while 750 nm is restricted. At D = 360 nm, transmission of 650 nm can be restricted, while 750 nm is transmitted. For the same geometry, the behavior can be reversed for different source angle. Fig.5.10(c) shows operation of 2×2 NPW as a color router for source inclined at 10º. The similar structure can be used as a mixer, where combination of the two

wavelengths can be obtained at the output ports when each input waveguide is excited with individual wavelength.

5.4 Fabrication and Experiment Procedure

The NPW devices can be fabricated using a planar or a non-planar device based on the simulation results obtained above. These devices are highly integrable to the silicon devices where plasmons can be excited using gratings or tapered waveguides. The waveguides can be closed structures (slot, coaxial etc.) or open (wedge, groove etc.). We propose in Fig.5.11 a novel bottom-up fabrication approach for a stand-alone planar NPW device, which can be fabricated using simple physical deposition and milling technique.

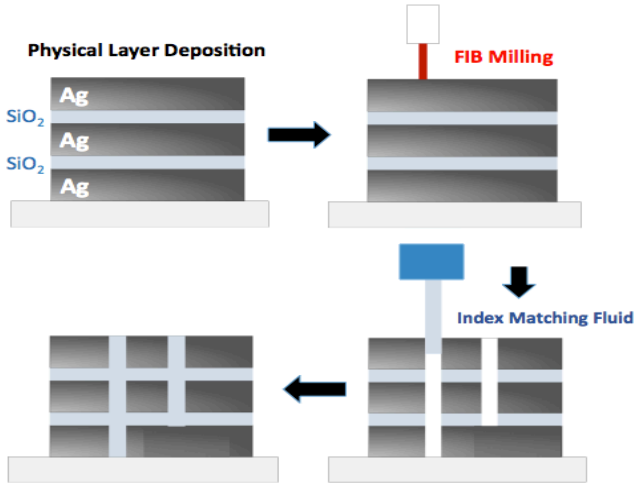

Fig.5.11: Schematic showing the proposed fabrication steps for 2 X 2 networked plasmonic devices.

The different device dimensions are to be fabricated based on the simulation results. The lateral x- dimensions would be kept high enough that the plasmons decay and the effect of reflection from open ends is negligible. For the experiment procedure we propose transmission spectroscopy technique using super-continuum and tunable laser source. The plasmons would be excited using end fire technique. As the two output ports are separated by distance smaller than the diffraction limit, the two outputs can be distinguished under the optical microscope; thus we plan to mill the second vertical waveguide partially through the

bottom Ag layer. The simulations confirmed that the output at output port 1 is minimally altered by partially milling the second port.

Fabricated Sample

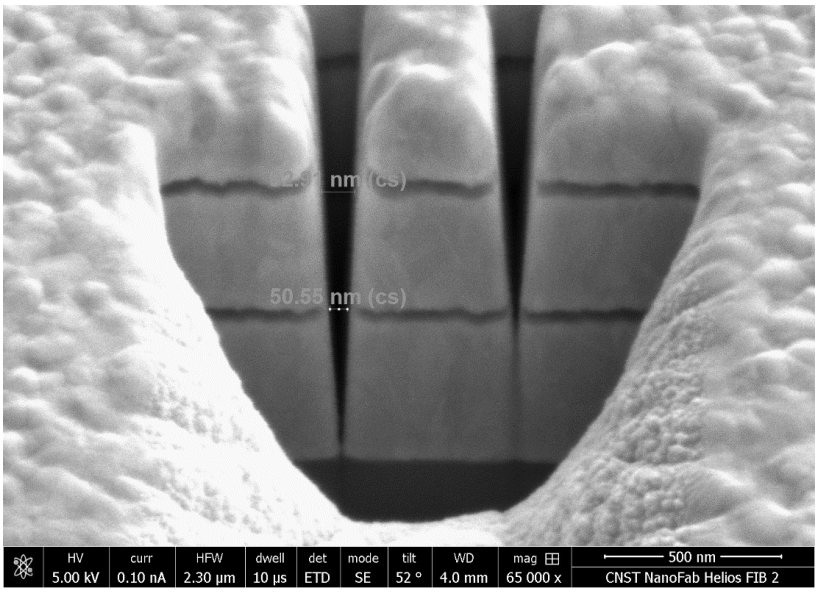

Fig.5.12: SEM image at 52º tilt angle for 2x2 NPW obtained through FIB milling tool. The fabricated sample shows a taper angle of ≃ 4º. The sample is fabricated for D=T=400 nm, W1=W2=30nm, W3=W4=100nm.

The simulations with the tapering in the vertical waveguides (Fig.5.12) showed that the general trend in the transmission plots still persists.

6 Summary and Future Work

Over the past few years, interest in plasmonics has revived with great vigor. Research in plasmonics has emerged to practical devices ranging from discrete to integrated devices, and from optical communication wavelengths to visible and ultraviolet. In this report we have investigated the behavior of surface plasmon polaritons at optical frequencies, determining the effective refractive index and dispersion curves for different width of metal-insulator-metal based plasmonic waveguide geometry. For the Ag-SiO_2-Ag geometry we found that as we squeeze the plasmons into smaller core dimensions, the wave-vector increases. To design effective and practical devices, we determined the propagation length and the plasmon decay rate with waveguide width for different optical frequencies. As the losses in metal (Silver in our case) increases at higher frequencies or lower wavelengths, we determined an optimal trade-off between operating frequency and the propagation length at 750 and 650 nm source wavelengths.

To lay foundation for plasmonic based integrated circuit devices we begin by developing generic design rules and challenges in basic plasmonic waveguide components. We found that plasmonic waveguide structures show similar response as transmission lines and the reflection and transmission through L-bend, T-bend and Side-port waveguides can be modeled by impendence matching, where effective impendence can be found using the effective refractive index for the waveguide geometries. We found that these conditions are satisfied when only when the effective wavelength of surface plasmon polariton is greater than the width of the waveguide. We also investigated the behavior of 4-port splitting devices and deduced that the structure behaves as an equal power splitting device as we go towards near infrared wavelength. For optical frequencies the reflection into the input port increases as we increase the waveguide width. Using these generic knowledge, we designed networked plasmonic

devices at optical frequencies which utilize the effect of interference between the intersecting waveguides. Due to this interference effect the output at the ports can easily be modulated. Using 2 X 2 Networked Plasmonic Waveguides (NPW), comprising of network of two parallel vertical and horizontal waveguides, we designed different devices for 750 nm and 650 nm source excitations. However, the plasmonic waveguide networks have already been proposed and designed for optical wavelengths in ref [12], where the modulation and tunability of device could be controlled. We propose here a novel approach to modulate the output at the ports by introducing a phase difference into the two input ports by changing the angle of source excitation. Based on the angle modulation for 2 X 2 NPW we designed devices like optical switch, directional filter and color routers. The plasmon waveguide network can also be used to enhance the absorption of light in photovoltaic devices by trapping and propagating the light along the absorption layer. The devices can also be effectively utilized for chemical and biological sensing where one vertical waveguide can be filled with sample under test.

The 2D simulation results obtained using FDTD technique could be effectively used to design planar discrete and integrated devices. As an initial step, we propose a fabrication technique for a stand-alone device where the devices would be fabricated using Focused Ion Beam milling into alternate Ag and SiO_2 layers. The devices are under fabrication and the experimental setup has been designed for transmission spectroscopy. We also plan to incorporate the directional control on light electro-optic technique.

References

[1]. J. Zenneck, "About the propagation of electromagnetic plane waves along a conductor plane and their relationship to wireless telegraphy," *Ann. der Physik*, **23**, 846--866 (1907).

[2]. R. W. Woods, "On a remarkable case of uneven distribution of light in a diffraction grating spectrum," *Phtl. Mag.* **4**, 396-402(1902).

[3]. R. Ritchie, "Surface-plasmon resonance effect in grating diffraction," *Phys. Rev. Lett.* **21**,530-1532(1968).

[4]. T.W. Ebbeson, H.J. Lezec, H.F. Ghaemi, T. Thio, and P.A. Wolff, "Extraordinary optical transmission through sub-wavelength hole arrays," *Nature* **391**, 667-669 (1998).

[5]. M. Fleischmann, P. J. Hendra, and A. J. McQuillan, "Raman spectra of pyridine adsorbed at a silver electrode," *Chem. Phys. Lett*. **26**, 163–166. (1974).

[6]. H.J Lezec, A. Degiron, E. Devaux, R. A. Linke, L. Martin-Moreno, F. J. Garcia-Vidal, and T.W. Ebbeson, "Beaming Light from a Subwavelength Aperture," *Science* **297**, 5582, 821-822 (2002).

[7]. A. Degiron and T. W. Ebbesen, "The role of localized surface plasmon modes in the enhanced transmission of periodic subwavelength apertures," *J. Opt. A: Pure Appl. Opt.* **7** S90 (2005).

[8]. T. Matsui, A. Agrawal, A. Nahata, and Z.V. Vardney, "Transmission resonances through aperiodic arrays of subwavelength apertures," *Nature* **446**, 517-521 (2007).

[9]. L. Dal Negro, N. Feng and A. Gopinath, "Electromagnetic coupling and plasmon localization in deterministic aperiodic arrays," *J. Opt. A* **10**, 064013 (2008).

[10]. J.C. Weeber, A. Dereux, C. Girard, J. R. Krenn, and J.P. Goudonnet, "Plasmon polaritons of metallic nanowires for controlling submicron propagation of light," *Physical Review B* **60**, (12), 9061-8 (1999).

[11]. B. Lamprecht; J. R. Krenn, G. Schider, H. Ditlbacher, M. Salerno, N. Felidj, A. Leitner, F. R. Aussenegg, and J. C. Weeber, "Surface plasmon propagation in microscale metal stripes," *Applied Physics Letters* **79**, (1), 51-3 (2001).

[12]. J. A. Dionne, H. J. Lezec, and H. A. Atwater, "Highly confined photon transport in subwavelength metallic slot waveguides," *Nano Letters* **6**, 1928 (2006).

[13]. E. Feigenbaum and H. A. Atwater, "Resonant guided wave networks," *Phys. Rev. Lett.* **104**, 147402 (2010).

[14]. M. L. Brongersma and V. M. Shalaev, "A case for plasmonics," *Science* 328, 5977, p. 440-441 (2010)**.**

[15]. N.W. Ashcroft and N.D. Mermin, *Solid-State Physics*, Saunders College (1976).

[16]. P.B. Johnson and R.W. Christy, "Optical constant of the noble metals," *Physical Review B* **6,** 12 (1972).

[17]. S. Maier, *Plasmonics: Fundamentals and Application*s, Springer (2007).

[18]. L. Novotny and B. Hecht, *Principles of Nano-optics*, Cambridge (2011).

[19]. W.L. Barnes, A. Dereux and T.W. Ebbesen, "Surface plasmon subwavelength optics," *Nature* **424**, 6950 (2003).

[20]. H. Raether, *Surface Plasmons on Smooth and Rough Surfaces and on Gratings*, Springer-Verlag (1986).

[21]. J. A. Dionne and H.A. Atwater, "Flatland Photonics: Circumventing diffraction with Planar Plasmonic Architectures," PhD Thesis, Caltech (2009).

[22]. E. N. Economou, "Surface plasmons in thin films", *Physical Review* **182**, 1 (1969).

[23]. A.V. Zayats, I. I. Smolyaninov, and A. A. Maradudin, "Nano-optics of surface plasmon polaritons," *Physics Reports* **408** (2005) 131–314(2005).

[24]. H. Ditlbacher, J.R. Krenn, N. Felidj, B. Lamprecht, G. Schider, M. Salerno, A. Leitner, and F.R. Aussenegg, "Two-dimensional optics with surface plasmon polaritons," *Applied Physics Letters*, **80**, 3, 404-406 (2002).

[25]. M. Moskovits, "Surface-enhanced spectroscopy," *Rev. Mod. Phys*. **57** (1985).

[26]. S. Ushioda, Y. Uehara, and M. Kuwahara, "STM light emission spectroscopy of Au film," *Appl. Surf. Sci*. **60** (1992).

[27]. C.F. Bohren and D.R. Huffman, *Absorption and Scattering of Light by Small Particles*, Wiley-Vch (2008)

[28]. J.B. Pendry, L. Martin-Moreno, and F. J. Garcia-Vidal, "Metamaterials and negative refractive index," *Science* **305**, 5685 (2004).

[29]. F. J. Garcia-Vidal and L. Martin-Moreno, "Surfaces with holes in them: new plasmonic metamaterials," *J. Opt. A: Pure Appl. Opt*. **7** (2005).

[30]. F. J. Garcia-Vidal and L. Martin-Moreno, "Transmission and focusing of light in one-dimensional periodically nanostructured metals," *Physical Review B* **66**, 155412 (2002).

[31]. H. A. Bethe, "Theory of diffraction by small holes*," Phys. Rev.* **66** 163–82 (1944).

[32]. A. Degiron, H.J. Lezec, N. Yamamoto, and T.W. Ebbesen, "Optical transmission properties of a single subwavelength aperture in a real metal", *Optics Communications* 239, 61-66 (2004).

[33]. G. Veronis, S.E. Kocabas, D.A.B. Miller, and S. Fan, "Modeling of plasmonic waveguide components and networks," *Journal of Computational and Theoretical Nanoscience* (2009).

[34]. A. Taflove and S. C. Hagness , *Computational Electrodynamics: The Finite Difference Time-Domain Method*, 3rd Ed, Artech House Publishers.

[35]. K. Yee, "Numerical solution of initial boundary value problems involving Maxwell's equations in isotropic media," *IEEE Transactions on Antennas and Propagation* **14** (3): 302–307 (1966).

[36]. K. C. Y. Huang, M. Seo, T. Sarmiento, Y. Huo, J. S. Harris, and M. L. Brongersma, "Electrically driven subwavelength optical nanocircuits," *Nature Photonics* **8**, 244–249 (2014).

[37]. A. Melikyan, L. Alloatti, A. Muslija, D. Hillerkuss, P. C. Schindler, J. Li, and J. Leuthold, "High-speed plasmonic phase modulators," *Nature Photonics* **8**, 229–233 (2014).

[38]. A. Christ, Tikhodeev, N. A. Gippius, J. Kuhl, and H. Giessen, "Waveguide-plasmon polaritons: Strong coupling of photonic and electronic resonances in a metallic photonic crystal slab," *Phys. Rev. Lett*. **91**, 183901 (2003)

[39]. L. Liu, Z. Han, and S. He, "Compact gradual bends for channel plasmon polaritons," *Optics Express* **13**, 17, 6645-6650 (2005).

[40]. J. A., Dionne, L. A. Sweatlock, H. A. Atwater, and A. Polman, "Plasmon slot waveguides: Towards chip-scale propagation with subwavelength-scale localization," *Physical Review B* **73**, 3 (2006).

[41]. W. Shin, W. Cai, P. B. Catrysse, G. Veronis, M. Brongersma, and S. Fan, "Broadband sharp 90-degree bends and T-splitters in plasmonic coaxial waveguides," *Nano letters*, ***13***(10), 4753-4758 (2013).

[42]. Y. Matsuzaki, T. Okamoto, M. Haraguchi, M. Fukui, and M. Nakagaki, "Characteristics of gap plasmon waveguide with stub structures," *Optics Express* **16**, 21, 16314-16325 (2008).

[43]. R. Zia, M. D. Selker, P. B. Catrysse, and M. Brongersma , "Geometries and materials for subwavelength surface plasmon modes," *J. Opt. Soc. Am.* **21**, 12 (2004)

[44]. H. Miyazaki and Y. Kurokawa, “Squeezing visible light waves into a 3-nm-thick and 55-nm-long plasmon cavity,” *Phys. Rev. Lett.* **96**, 097401 (2006).

Vita

ASHISH CHANANA

Present Address
1027 E Genesee Street
Syracuse, NY 13210

achanana@syr.edu
(917) 767 8654

Education

Syracuse University — Syracuse, NY
M.S. in Electrical Engineering — June, 2015
GPA 3.792 / 4.0

Maharshi Dayanand University
Manav Rachna College of Engineering — Haryana, India
B.Tech., Electrical and Communications Eng. — July, 2011
GPA: 3.9/4.0(1st Division, Hons. Degree)

Research Experience

Research Assistant — Aug, 2014-Present
Multiscale Research & Engineering Laboratory, Syracuse University
Advisor: Dr. Shalabh Maroo

- Measurement of contact angle of bubble in pool boiling
- Detection and measurement of thin film of non-evaporating layer in pool boiling using Michelson Interferometer

Research Assistant and Lab Coordinator — Nov, 2013-Aug,2014
Nanophotonics Lab, Syracuse University
Advisor: Prof. Amit Agrawal

- Facilitated spectroscopy experimental setup for plasmonic devices. Conducted measurements of transmission and reflection spectrum. Designed microscope stage for directional light incidence

Research Intern — July, 2011-Mar, 2012
Magnetic Standards and Materials, National Physical Laboratory, New Delhi, India
Advisor: Dr. R.K. Kotnala

- Synthesized and characterized (AFM and SEM) Lanthanum strontium manganite (LSMO) with varied copper and zinc doping concentration. Studied the electric and magnetic properties
- Studied magnetic properties of LSMO and Bismuth Ferrite (BFO) using Vibrational magnetometer

Professional Experience

Software Engineer — *Mar, 2012-Jan,2013*
Tata Consultancy Services Ltd., New Delhi

Publications

- Ashish Chanana, Jay K. Lee, Henri Lezec, Amit Agrawal, 'Guided-wave Nanophotonic Devices based on Networked Plasmonic Waveguides ' (in progress-to be submitted in Jan-Feb'15)
- Ashish Chanana, An Zou, Amit Agrawal, Shalabh Maroo, 'Steady state stable bubble in pool boiling' (submitted)
- Ashish Chanana, An Zou Amit Agrawal, Peter C. Wayner, Shalabh Maroo, 'Contact Angle Measurement of Vapour Bubble in Pool Boiling', 9th International Conference on Boiling and Condensation Heat Transfer, April 2015